nature communications

Article

https://doi.org/10.1038/s41467-026-74740-3

Dipeptidyl peptidase 3 sets the threshold for immune activation and survival during experimental bacterial infection

Received: 25 July 2025

Accepted: 15 June 2026

Published online: 06 July 2026

Check for updates

Amanda Facoetti[1,2,16], Luca Lambroia[3,16], Elena Fontana[2], Federico Nicchiotti[2,4], Maria Lucia Schiavone[2], Dario Strina[2,5], Raffaello Viganò[6], Francesca Brambilla[6], Davide Mangioni[7], Samantha Scaramuzza[8], Sara Mallia[9], Marcella Bonanomi[9], Andrea Farini[10], Mirella Meregalli[11], Debora Mostosi[10,11], Giuseppe Rocca[12], Ciro Menale[2,13], Cecilia Garlanda[1,2], Antonio Muscatello[7], Alessandra Bandera[7,14], Daniela Gaglio[9], Cristina Sobacchi[2,5], Yvan Torrente[10,11], Pierluigi Mauri[6], Dario Di Silvestre[6], Clelia Peano[5,15], Francesca Granucci[12], Veronica Marrella[2,5,17] & Barbara Cassani[2,4,17]

Effective host defense requires coordinated regulation of immune activation, metabolism, and redox balance, yet how these processes are integrated remains unclear. Here, we identify dipeptidyl peptidase 3 (Dpp3) as a regulator of immune activation thresholds during bacterial infection. *Dpp3*−/− mice display enhanced resistance to *Klebsiella pneumoniae*, with early divergence in bacterial burden, improved survival, preserved tissue architecture, and reduced systemic inflammation. Adoptive transfer experiments demonstrate that Dpp3-deficient immune cells are sufficient to confer protection, indicating a cell-intrinsic effect. Mechanistically, Dpp3 deficiency impairs inducible Nrf2 stabilization, resulting in amplified ROS accumulation and enhanced NF-κB–associated responses. Integrated metabolomic, bioenergetic, and proteomic analyses reveal coordinated mitochondrial remodeling and activation of inflammatory signaling networks, consistent with a metabolically primed immune state. Collectively, these findings establish Dpp3 as a systems-level regulator integrating redox control and immunometabolism to calibrate antimicrobial responses during infection.

Bacterial infections, particularly when accompanied by dysregulated host response and organ dysfunction (i.e., sepsis), remain a leading cause of morbidity and mortality worldwide despite advances in supportive care and antimicrobial therapy[1]. Clinical outcome in sepsis is determined by the balance between resistance and tolerance: insufficient immune activation permits pathogen dissemination, whereas excessive inflammation drives tissue injury, organ dysfunction, and mortality[2,3].

Effective host defense requires immune cells to coordinate inflammatory signaling with metabolic adaptation and redox control[4]. However, the molecular mechanisms that integrate these processes to define immune activation thresholds remain incompletely understood.

Reactive oxygen species (ROS) function as key second messengers in innate and adaptive immunity, shaping immune activation and antimicrobial responses[5]. To preserve redox homeostasis, immune cells rely on the transcription factor Nrf2 (nuclear factor erythroid 2-related factor 2), a central regulator of antioxidant gene expression[6]. Beyond controlling oxidative stress, Nrf2 intersects with

A full list of affiliations appears at the end of the paper. e-mail: barbara.cassani@unimi.it

immunometabolic circuits that sustain effector function[7,8]. Loss of Nrf2 activity has been linked to dysregulated inflammation and impaired host defense[9,10]. Although the downstream transcriptional programs governed by Nrf2 are well characterized, upstream modulators that fine-tune inducible Nrf2 activation in immune cells remain less clearly defined.

Dipeptidyl peptidase 3 (Dpp3) is a cytosolic zinc-dependent aminopeptidase that degrades dipeptides and bioactive peptides, including angiotensin II (Ang II)[11–13]. Beyond its enzymatic activity, Dpp3 has been reported to interact with KEAP1, the principal inhibitor of Nrf2, suggesting a role in modulating redox-sensitive signaling[14,15]. Elevated circulating Dpp3 levels are associated with poor prognosis in sepsis and cardiogenic shock[16,17], implicating Dpp3 in critical illness. However, whether Dpp3 directly regulates immune activation during infection remains unknown.

Dpp3 is broadly expressed across multiple mammalian tissues, including metabolic, cardiovascular, and hematopoietic compartments such as bone marrow and spleen, consistent with its classification as a ubiquitously distributed zinc-dependent aminopeptidase[13,18]. Its presence in immune-related organs raises the possibility that Dpp3 integrates immune-intrinsic and systemic responses during infection, yet the functional relevance of this widespread expression in host defense has not been defined.

Here, we investigate the role of Dpp3 in immune regulation during bacterial infection using genetic loss-of-function models of pulmonary and systemic challenge. We demonstrate that Dpp3 deficiency enhances bacterial clearance and improves survival while limiting tissue injury. Through integrated in vivo, transcriptomic, biochemical, metabolic, and proteomic analyses, we identify Dpp3 as a regulator of immune activation thresholds that coordinates redox control, proteostasis, and inflammatory signaling during infection.

Results

Systemic Dpp3 levels increase during *K. pneumoniae* infection

Current knowledge of Dpp3 in infection is largely derived from critically ill patients[19,20], yet its functional role in bacterial pathophysiology remains unclear. We first examined whether Dpp3 is regulated during infection. Plasma Dpp3 concentrations were significantly elevated in patients with non-bacteraemic *Klebsiella pneumoniae* carbapenemase-producing (KPC-*Kp*) infection compared to both healthy controls and colonized individuals (Supplementary Fig. 1A), suggesting an association with active disease.

To explore this observation experimentally, wild-type (WT) mice were intranasally infected with 2×10^2 CFU of *Kp* [21]. Circulating Dpp3 levels were significantly increased at 20 and 48 h post infection (Supplementary Fig. 1B), corresponding to the phase of bacterial expansion and systemic dissemination (Fig. 1A, B), and declined toward baseline by day 10 during infection resolution (Supplementary Fig. 1B; and Fig. 1C). These findings identify Dpp3 as a dynamically regulated marker of infection and support a potential functional role during host–pathogen interactions.

Dpp3 deficiency enhances pulmonary defense in experimental pneumonia

Dpp3−/− mice[15] were used to determine whether Dpp3 contributes to host defense against *Kp* infection. As early as 8 h post-intranasal infection, *Dpp3*−/− mice exhibited significantly reduced pulmonary bacterial burden compared to WT controls, an effect that persisted at 48 h (Fig. 1A). Dpp3 deficiency also limited systemic dissemination, as reflected by a lower frequency of bacteremia (Fig. 1B) and more than a ten-fold reduction in circulating bacterial load at 48 h post-infection (5298 ± 620 CFU ml^{-1} in *Dpp3*−/− vs 41990 ± 4222 CFU ml^{-1} in WT; $p = 0.0298$). Consistently, survival was significantly improved in *Dpp3*−/− mice (87.5% vs 58% at day 10; $p = 0.044$) (Fig. 1C), indicating enhanced resistance to *Kp*-induced pneumosepsis.

To assess whether improved bacterial control was associated with altered inflammatory responses, we first examined early inflammatory signaling in the lung. At 8 h post-infection, quantitative PCR analysis revealed modulation of *Myd88, Tlr4*, and *NF-kB* expression in *Dpp3*−/− mice compared to WT controls (Fig. 1D), indicating early divergence in TLR/NF-κB-associated pathways. We next quantified cytokines and chemokines in lung homogenates at 48 h post-infection. As shown in Fig. 1E, infected *Dpp3*−/− mice exhibited significantly reduced levels of IL-6, IL-1β, CXCL1 compared to WT counterparts, with additional non-significant trends toward lower TNF, IL-17, CXCL2, CCL4, CCL3, CXCL10 and MPO, and modest increases in GM-CSF, IFN-γ and IL-10 (Fig. 1E; Supplementary Table 1). These data indicate that early transcriptional differences are accompanied by a distinct inflammatory milieu at later stages of infection.

Histopathological analysis of lungs at 48 h post-infection revealed markedly attenuated parenchymal injury in *Dpp3*−/− mice. WT lungs displayed diffuse interstitial inflammation, suppurative bronchopneumonia, and alveolar hemorrhage, accompanied by dense MPO$^+$ neutrophilic infiltrates forming focal inflammatory aggregates (Fig. 1F, G). In contrast, *Dpp3*−/− lungs maintained preserved architecture, reduced inflammatory lesions, and decreased polymorphonuclear cell (PMN) infiltration (Fig. 1F, G), indicating that enhanced antimicrobial defense occurred without exacerbated neutrophilic damage. Consistently, CD31 immunostaining demonstrated reduced inflammatory angiogenesis[22] in *Dpp3*−/− lungs (Supplementary Fig. 2A, B). Although mononuclear cell (MNC) infiltration was comparable between genotypes (Fig. 1G), *Dpp3*−/− lungs exhibited increased Iba1$^+$ macrophage abundance and more organized adaptive immune architecture, including structured B- and T-cell aggregates (Supplementary Figs. 2C–E and 3A–C). Notably, these structural features were already evident in naive *Dpp3*−/− lungs, consistent with an altered baseline immune set-point.

To assess the functional state of lung immune cells, ex vivo analyses were performed on cells isolated from infected lungs.

CD45$^+$ lung cells from Dpp3−/− mice exhibited increased expression of the transcription factors *Tbx1, Stat1*, and *Irf8* following *K. pneumoniae* infection, consistent with activation of antimicrobial and immune-regulatory transcriptional programs (Supplementary Fig. 3D). In line with this transcriptional profile, CD11b$^+$ cells from *Dpp3*−/− mice displayed enhanced phagocytic activity, as measured by FITC-bead uptake, along with increased ROS production and elevated MHC class II expression, indicating augmented antimicrobial and antigen-presenting capacity (Supplementary Fig. 3E–G). In parallel, *Dpp3*−/− lungs showed increased frequencies of germinal center and CD138$^+$ plasma cells (Supplementary Fig. 3H, I), as well as expanded effector memory (EM) CD4$^+$ and CD8$^+$ T-cell populations and higher proportions of proliferating Ki67$^+$ T cells (Supplementary Fig. 3J, K). Together, these findings support enhanced functional activation of both innate and adaptive immune compartments in *Dpp3*−/− lungs following infection.

Flow cytometric analysis of lung immune populations (Supplementary Fig. 4) confirmed increased CD45$^+$ leukocyte recruitment following infection in both genotypes; however, the increase reached statistical significance only in WT lungs relative to baseline (Fig. 1H). WT mice also displayed a concomitant reduction in circulating immune cells, indicative of peripheral-to-pulmonary redistribution, whereas *Dpp3*−/− mice maintained stable peripheral counts (Fig. 1I). Both innate and adaptive subsets expanded in infected WT lungs, while these increases were attenuated in *Dpp3*−/− counterparts (Fig. 1H), consistent with higher basal immune cell abundance in *Dpp3*−/− lungs under steady-state conditions. Adaptive responses were evaluated by measuring circulating immunoglobulins (Ig). Circulating IgM, IgA, and IgG2b levels, relevant for defense against encapsulated and mucosal pathogens, were significantly elevated in *Dpp3*−/− mice compared to WT animals (Fig. 1J). In line with attenuated systemic inflammation,

https://doi.org/10.1038/s41467-026-74740-3

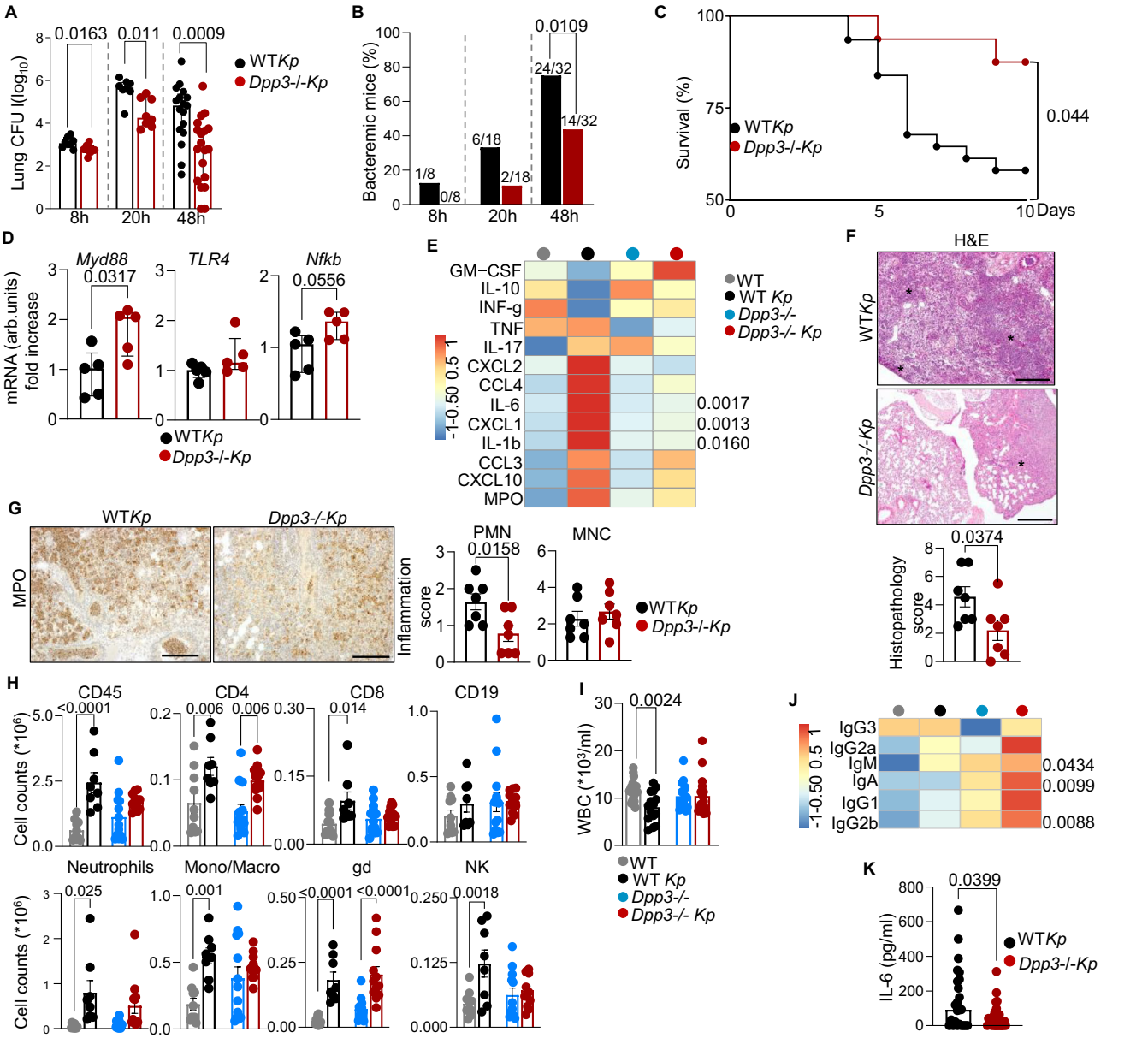


Fig. 1 | Dpp3 deficiency enhances pulmonary bacterial control. A Pulmonary bacterial burden in WT and *Dpp3*−/− mice at 8 h (WT $n = 8$, 5 M 3 F; *Dpp3*−/− $n = 8$, 3 M 5 F), 20 h (WT $n = 8$, 4 M 4 F; *Dpp3*−/− $n = 8$, 4 M 4 F), and 48 h (WT $n = 17$, 10 M 7 F; *Dpp3*−/− $n = 19$, 12 M 7 F) following intranasal infection with 2×10^2 CFU of *Kp*. **B** Frequency of bacteremic mice at the indicated time points; numbers above bars indicate bacteremic/total mice per group. **C** Kaplan–Meier survival analysis of WT ($n = 31$, 20 M 11 F) and *Dpp3*−/− ($n = 22$, 12 M 10 F) mice monitored until day 10 post-infection. **D** Relative mRNA expression in lung tissue at 8 h post-infection, expressed as fold change relative to basal levels ($n = 5$ biological replicates for each group). **E** Heatmap of cytokine and chemokine levels in lung homogenates at 48 h post-infection ($n \geq 6$ biological replicates). Values represent median-centered log-transformed z-scores; Average and Sdev are provided in Supplementary Table 1. Significant differences between WT Kp and *Dpp3*−/− Kp are indicated. **F** Representative H&E staining of WT and *Dpp3*−/− mice lung sections (×4; scale bar, 500 µm) and corresponding histopathology scores ($n = 7$ biological replicates for each group). Asterisks indicate areas enriched in neutrophilic infiltration. **G** MPO immunohistochemistry (×4; scale bar, 500 µm) with corresponding inflammation scores based on PMN and MNC infiltration at 48 h ($n = 7$ biological replicates for each group). **H** Cell counts of lung immune populations assessed by FACS in the indicated groups at 48 h (biological replicates: WT, $n = 10$; WT *Kp*, $n = 13$; *Dpp3*−/−, $n = 8$; *Dpp3*−/− *Kp*, $n = 12$). **I** White blood cell count obtained by haemocytometer from indicated groups of mice at 48 h (biological replicates: WT, $n = 21$; WT *Kp*, $n = 15$; *Dpp3*−/−, $n = 18$; *Dpp3*−/− *Kp*, $n = 17$). **J** Heatmap of Ig serum levels at 48 h ($n = 5$ biological replicates for each group). **K** Plasma IL-6 levels at 48 h (biological replicates: WT Kp, $n = 24$ *Dpp3*−/− *Kp*, $n = 28$). Data are shown as individual points with mean ± SEM (parametric) or median ± IQR (non-parametric). Statistical analysis: unpaired two-tailed Student's *t* test (**F, G**), unpaired two-tailed Mann–Whitney *U* test (**A**, **D**, **K**), two-way ANOVA (**E**, **H**,–**J**), Chi-square test (**B**), and log-rank test (**C**). Data represent representative or pooled results from at least two independent experiments. Source data are provided as a Source Data file.

plasma IL-6 concentrations were significantly reduced in *Dpp3*−/− animals (Fig. 1K).

By day 10 post-infection, pulmonary bacterial burden was markedly lower in both genotypes and nearly undetectable in *Dpp3*−/− mice (Supplementary Fig. 5A, B), consistent with effective infection control. Plasma IL-6 levels had declined, and pulmonary hemorrhagic lesions were no longer detectable in surviving animals (Supplementary Fig. 5C), indicating resolution of acute inflammatory injury. In *Dpp3*−/− mice, immune infiltrates persisted without overt tissue damage, suggesting sustained but controlled immune activity during recovery (Supplementary Fig. 5D, E). Collectively, these findings demonstrate that Dpp3 deficiency enhances bacterial clearance while limiting

infection-induced tissue injury, consistent with improved immune efficiency rather than hyperinflammation.

To assess whether the protective phenotype of Dpp3 deficiency extended beyond a single pathogen, WT and *Dpp3*−/− mice were intranasally challenged with *Pseudomonas aeruginosa* (PAO1). *Dpp3*−/− mice exhibited significantly reduced pulmonary bacterial burden at 48 h post-infection (Supplementary Fig. 6A), accompanied by attenuated lung injury with lower peribronchial inflammation and reduced leukocyte accumulation (Supplementary Fig. 6B). While PMN cell recruitment was decreased, MNC infiltration was increased in *Dpp3*−/− lungs (Supplementary Fig. 6C, D). This shift in inflammatory composition was paralleled by reduced local and systemic IL-6 levels (Supplementary Fig. 6E, F), indicating that the protective phenotype extends across distinct Gram-negative pulmonary infections.

Dpp3 deficiency improves systemic host defense during sepsis

Building on the protective phenotype observed in pulmonary infection, we next assessed whether Dpp3 deficiency confers systemic protection in a model of intraperitoneal *Kp* challenge. At 48 h post-infection, *Dpp3*−/− mice exhibited significantly reduced bacterial burden in liver homogenates compared with WT controls (Fig. 2A), indicating enhanced systemic bacterial clearance.

Histological examination of lungs revealed attenuated tissue injury in *Dpp3*−/− mice (Fig. 2B), with reduced bronchial, alveolar, and vascular hemorrhage. Semi-quantitative scoring confirmed significantly lower histopathology scores in Dpp3-deficient animals (Fig. 2C, D), supporting reduced systemic inflammatory damage.

To assess inflammatory effector responses, we analyzed ROS production and lipid mediators. Splenic CD11b+ cells from *Dpp3*−/− mice displayed significantly increased intracellular ROS levels compared to WT animals (Fig. 2E), indicating enhanced oxidative activation. Consistent with amplified neutrophil effector function[23], serum LTB4 concentrations were elevated in *Dpp3*−/− mice (Fig. 2F).

Immune cell composition in the peritoneal cavity was then assessed. *Dpp3*−/− mice exhibited increased frequencies of $CD3^+$ T cells and $CD19^+$ B cells compared to WT controls (Fig. 2G), indicating heightened adaptive immune recruitment. Within the T-cell compartment, both $CD4^+$ and $CD8^+$ EM subsets were expanded (Fig. 2H).

Consistent with enhanced humoral activation, *Dpp3*−/− mice showed increased germinal center B cells (PNA^+FAS^+; Fig. 2I, J) and elevated frequencies of $CD138^+$ plasma cells (Fig. 2K). Circulating Ig levels were differentially modulated, with increased IgM, IgA and IgG2 detected in Dpp3-deficient animals (Fig. 2L). Upon stimulation, ex vivo splenocytes from infected *Dpp3*−/− mice showed significantly greater proliferation (Supplementary Fig. 7A), in line with elevated expression of TLR4 pathway components, including *Myd88* and downstream *NF-kB*(Supplementary Fig. 7B). Overall, these findings indicate that Dpp3 deficiency promotes systemic immune activation in response to infection.

Finally, systemic inflammatory markers were assessed. Plasma IL-6 levels were reduced in *Dpp3*−/− mice (Fig. 2M), indicating attenuated systemic inflammation. In contrast, circulating Ang II concentrations were significantly elevated in septic *Dpp3*-deficient animals compared to WT controls (Fig. 2N). As Dpp3 is known to degrade Ang II[24], this increase is consistent with reduced Ang II turnover during infection. Notably, WT mice displayed a marked rise in circulating Dpp3 levels under inflammatory conditions (Supplementary Fig. 7C), whereas no genotype-dependent differences in Ang II were observed at baseline (Mean ± SDev: WT 276.4 ± 110.7 vs. *Dpp3*−/− 259 ± 78.3 ng/ml), suggesting that Dpp3-mediated Ang II modulation is infection-dependent. In parallel, *Dpp3*−/− splenocytes exhibited increased expression of the Ang II receptor AT1R (Supplementary Fig. 7D), indicating enhanced responsiveness to Ang II signaling.

To functionally assess the contribution of AT1R signaling, *Dpp3*−/− mice were treated with the AT1R antagonist losartan during systemic infection (Supplementary Fig. 8A). AT1R blockade slightly increased bacterial burden in *Dpp3*−/− mice partially reversing the enhanced bacterial clearance observed in untreated knockout animals (Supplementary Fig. 8B). Histological analysis revealed worsened lung injury following losartan treatment (Supplementary Fig. 8C), accompanied by reduced ROS production (Supplementary Fig. 8D) and decreased LTB4 levels (Supplementary Fig. 8E). In parallel, alterations in effector T-cell subsets and plasma cell frequencies were observed (Supplementary Fig. 8F, G), consistent with dampened immune activation.

In contrast, losartan treatment had no significant effect on bacterial burden or inflammatory parameters in WT mice, indicating that the protective phenotype of Dpp3 deficiency is, at least in part, dependent on intact Ang II–AT1R signaling. These findings support the concept that Dpp3 modulates systemic antibacterial defense within a hormonal context that integrates immune activation and vascular signaling during sepsis.

Immune-intrinsic protection via adoptive transfer of splenocytes

Having established that Dpp3 deficiency improves systemic host defense, we next asked whether immune cells are intrinsically programmed to confer enhanced protection. We therefore characterized splenic immune subsets from WT and *Dpp3*−/− mice prior to adoptive transfer.

Dpp3−/− splenocytes displayed features consistent with a primed activation state. Total splenocytes exhibited increased phagocytic activity, with enhanced particle uptake by $CD11b^+$ cells relative to WT controls (Fig. 3A). Consistent with an activated antigen-presenting phenotype, $CD11b^+$ cells from *Dpp3*−/− mice also showed increased surface expression of MHC class II (Fig. 3B). Peripheral B-cell responses were similarly augmented, with elevated expression of *Prdm1* and *Xbp1* (Fig. 3C), increased frequencies of $CD138^+$ plasma cells (Fig. 3D), and expansion of germinal center B cells (PNA^+FAS^+; Fig. 3E) accompanied by increased *Aid* expression (Fig. 3C).

Peripheral T-cell populations in *Dpp3*−/− mice displayed an activated phenotype, including increased expression of *Tbx21, Blimp1*, and *Ccl3* (Fig. 3F), expansion of EM ($CD62L^-CD44^+$) and terminal effector (TE; $CD62L^-CD44^-$) subsets (Fig. 3G), increased proliferation and IFN-γ production (Fig. 3I, J), and an enlarged Treg compartment (Fig. 3H). Collectively, these findings indicate that Dpp3 deficiency is associated with a systemically primed immune state under steady-state conditions.

To determine whether this immune profile was sufficient to confer enhanced antibacterial defense, we performed adoptive transfer experiments in *Rag1*−/− recipients. Total splenocytes from WT or *Dpp3*−/− donors were intravenously transferred, followed by intranasal *Kp* infection 16 h later (Fig. 3K). Flow cytometric analysis confirmed successful homing of donor-derived T and B cells to the lung, whereas donor-derived $CD11b^+$ myeloid cells were detected at lower frequencies (Fig. 3L).

At 48 h post-infection, *Rag1*−/− mice receiving *Dpp3*−/− splenocytes exhibited significantly reduced pulmonary bacterial burden (Fig. 3M), diminished systemic dissemination (Fig. 3N), and lower local and systemic IL-6 levels (Fig. 3O, P) compared to recipients reconstituted with WT splenocytes. Together, these results show that Dpp3-deficient immune cells contribute to enhanced anti-bacterial protection in vivo.

Dpp3 is inducible in immune subsets in vivo during infection

Given that immune cells were crucial to transfer protection, we next examined the cellular distribution and inducibility of Dpp3. Quantitative RT-PCR of sorted pulmonary populations revealed significantly higher *Dpp3* transcript levels in immune cells compared to endothelial or epithelial compartments (Fig. 4A). Consistent with these findings, analysis of publicly available single-cell RNA-seq datasets[25]

https://doi.org/10.1038/s41467-026-74740-3

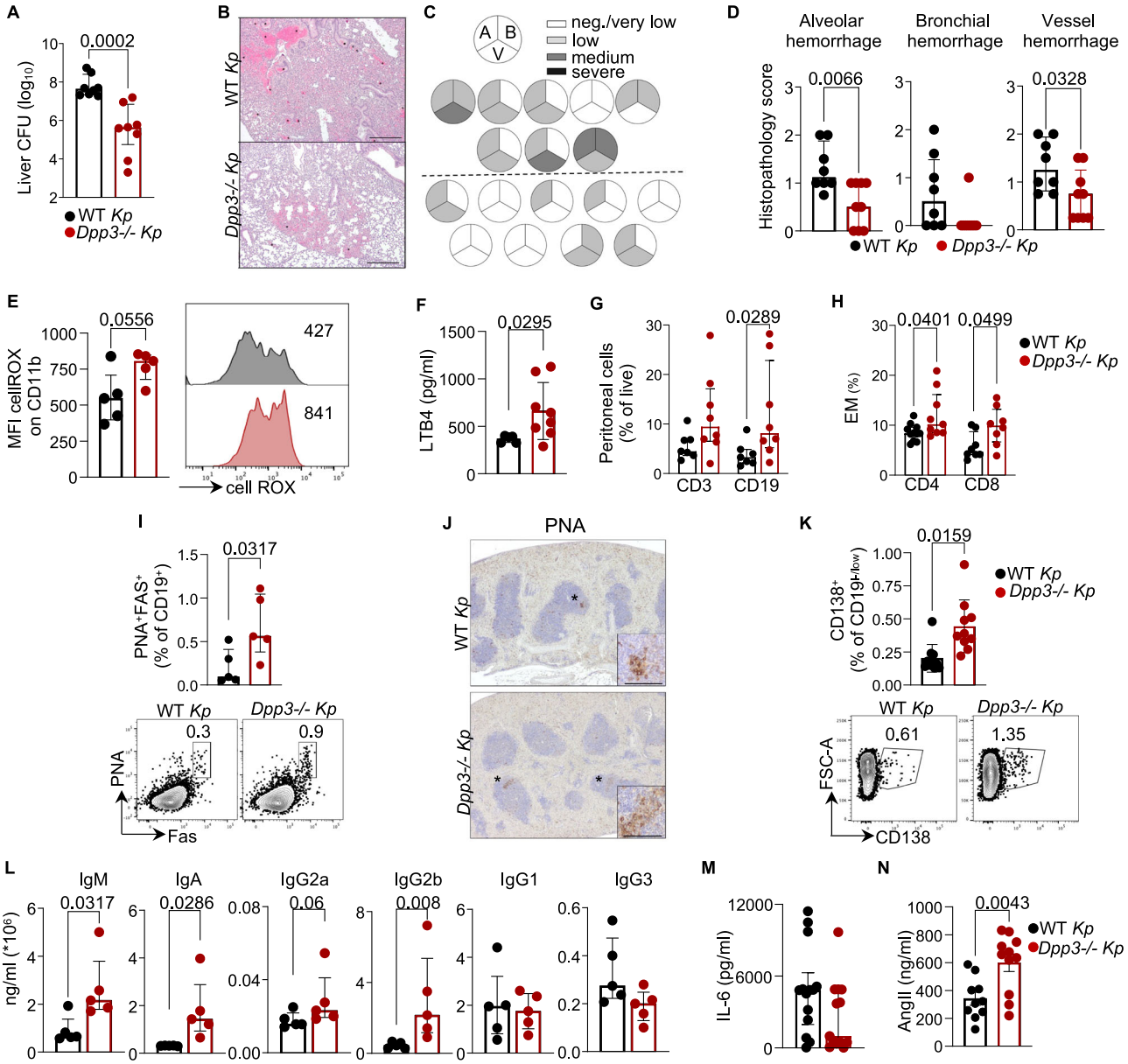


Fig. 2 | Dpp3 deficiency improves systemic antibacterial defense. A Bacterial burden in liver homogenates from WT and *Dpp3−/−* mice at 48 h following i.p. infection with *Kp* (WT $n = 8$, 5 M 3 F; *Dpp3−/−* $n = 8$, 4 M 4 F). **B** Representative H&E staining of WT and *Dpp3−/−* infected lung (×4; scale bar, 500 µm). **C** Distribution of alveolar (A), bronchiolar (B), and vascular (V) hemorrhagic damage scores in individual infected WT or *Dpp3−/−* mouse. **D** Quantification of histopathology score for single parameter contributing to lung damage in infected mice (biological replicates: WT, $n = 8$; *Dpp3−/−*, $n = 9$). **E** Intracellular ROS production from WT and *Dpp3−/−* splenic CD11b$^+$ cells 48 h post-infection, measured by FACS and shown as representative histograms and cumulative MFI ($n = 5$ biological replicates for each group). **F** LTB4 levels in sera 48 h post-infection (biological replicates: WT, $n = 5$; *Dpp3−/−*, $n = 8$). **G** Frequencies of CD3$^+$ and CD19$^+$ cells analyzed by FACS in peritoneal wash of infected mice (biological replicates: WT, $n = 7$; *Dpp3−/−*, $n = 8$). **H** FACS analysis of EM subset in splenic CD4$^+$ and CD8$^+$ cells from indicated groups of mice (biological replicates: WT, $n = 8$; *Dpp3−/−*, $n = 9$). **I** Frequencies of splenic germinal center (PNA$^+$FAS$^+$) B cells by FACS with representative dot plots ($n = 5$ biological replicates for each group). **J** Representative PNA immunostaining (×4; scale bar, 500 µm) of spleen sections (asterisks indicate germinal center structure with insets showing a ×20 magnification). **K** Frequencies of splenic CD138$^+$ plasma cells by FACS at 48 h post-infection and representative FACS dot plots (n = 10 biological replicates for each group). Plasma levels of immunoglobulin isotypes (**L**) ($n = 5$ biological replicates for each group); IL-6 (**M**) ($n = 16$ biological replicates for each group) and Ang II (**N**) ($n = 10$ biological replicates for each group) in WT and *Dpp3−/−* mice 48 h post-infection by ELISA. Data are presented as individual points with mean ± SEM (parametric) or median ± IQR (non-parametric), as indicated. Statistical analysis was performed using unpaired two-tailed Student's *t* test (**N**) or unpaired two-tailed Mann–Whitney *U* test (**A**, **D**–**M**), as appropriate. Exact *P* values are indicated. Data represent representative or pooled results from at least two independent experiments. Source data are provided as a Source Data file.

confirmed broad *Dpp3* expression across immune-lineage populations (Fig. 4B, C).

Ex vivo LPS stimulation of total splenocytes resulted in a significant increase in *Dpp3* mRNA levels (Fig. 4D) and an increased frequency of Dpp3$^+$ cells by immunofluorescence (Fig. 4E), demonstrating stimulus-dependent regulation. To determine whether Dpp3 upregulation occurs within specific immune subsets during in vivo infection, we analyzed protein expression by immunofluorescence staining in sorted splenic CD11b$^+$, CD19$^+$, and CD3$^+$ populations following intraperitoneal *Kp* challenge. Dpp3 expression increased significantly in all three subsets compared to naive controls, with the most pronounced induction observed in CD3$^+$ T cells (Fig. 4F). Together, these findings indicate that

https://doi.org/10.1038/s41467-026-74740-3

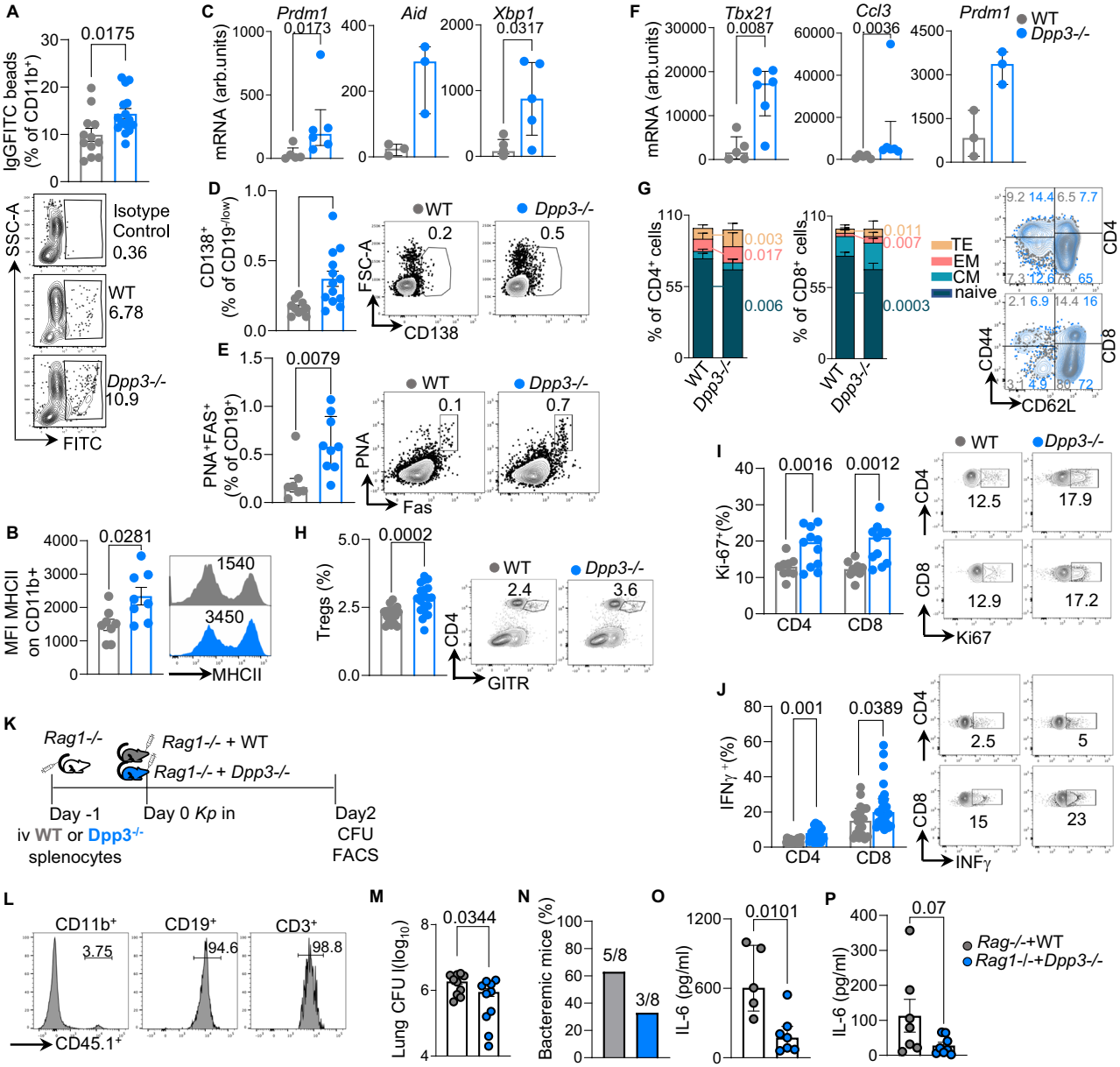


Fig. 3 | Adoptive transfer reveals immune-intrinsic protection. A Phagocytic capacity of WT and *Dpp3*−/− CD11b$^+$ splenocytes, expressed as the percentage of cells incorporating fluorescent beads (biological replicates: WT, $n = 12$; *Dpp3*−/−, $n = 15$). Representative dot plots and isotype controls are shown. **B** MFI expression of MHC class II on splenic CD11b$^+$ cells and representative FACS histogram ($n = 8$ biological replicates per group). **C** mRNA expression of plasma cell differentiation genes in sorted CD19$^+$ splenocytes (biological replicates: WT, $n = 3$; *Dpp3*−/−, $n = 5$). Histograms of frequencies and representative FACS dot plots of splenic CD138$^+$ plasma cells (biological replicates: WT, $n = 10$; *Dpp3*−/−, $n = 13$) (**D**) and germinal centers (PNA$^+$Fas$^+$; biological replicates: WT, $n = 7$; *Dpp3*−/−, $n = 9$) (**E**). **F** mRNA expression of effector-associated genes in sorted CD3$^+$ splenocytes (biological replicates: WT, $n = 5$; *Dpp3*−/−, $n = 6$). **G** Distribution of naive, EM, central memory (CM), and terminal effector (TE) subsets within CD4$^+$ and CD8$^+$ T cells (n = 23 biological replicates per group). Representative merged FACS dot plot for WT and *Dpp3*−/− mice is shown. **H** FACS analysis of CD4$^+$GITR$^+$ regulatory T cells (Tregs) (biological replicates: WT, $n = 18$; *Dpp3*−/−, $n = 21$)and Ki67$^+$ proliferating T cells (**I**) (biological replicates: WT, $n = 9$; *Dpp3*−/−, $n = 11$). Histograms of frequencies and a representative dot plot are shown. **J** Intracellular IFN-γ expression following PMA stimulation (biological replicates: WT, $n = 19$; *Dpp3*−/−, $n = 23$). Representative FACS plots are shown in selected panels. **K** Schematic of adoptive transfer: total splenocytes from WT or *Dpp3*−/− donors were intravenously injected into *Rag1*−/ − recipients. Cartoon mouse icon created with Microsoft PowerPoint. **L** Engraftment of CD45.1$^+$ donor-derived cells in the lung of *Rag1*−/− (CD45.2) recipients. **M** Pulmonary bacterial burden in reconstituted *Rag1*−/− mice ($n = 10$ biological replicates per group) following *Kp* infection. **N** Frequency of bacteremic recipient mice. **O** IL-6 levels in lung homogenates (biological replicates: WT, $n = 5$; *Dpp3*−/−, $n = 7$) and in serum (**P**) (biological replicates: WT, $n = 7$; *Dpp3*−/−, $n = 8$). Data are shown as individual points with mean ± SEM (parametric) or median ± IQR (non-parametric). Statistical analyses: unpaired two-tailed Student's *t* test (**A**, **D**, **I**, **M**, **P**), unpaired two-tailed Mann–Whitney *U* test (**B**, **C**, **E**–**H**, **J**, **O**), and Chi-square test (**N**). Exact *P* values are indicated. Data represent representative or pooled results from at least two independent experiments. Source data are provided as a Source Data file.

https://doi.org/10.1038/s41467-026-74740-3

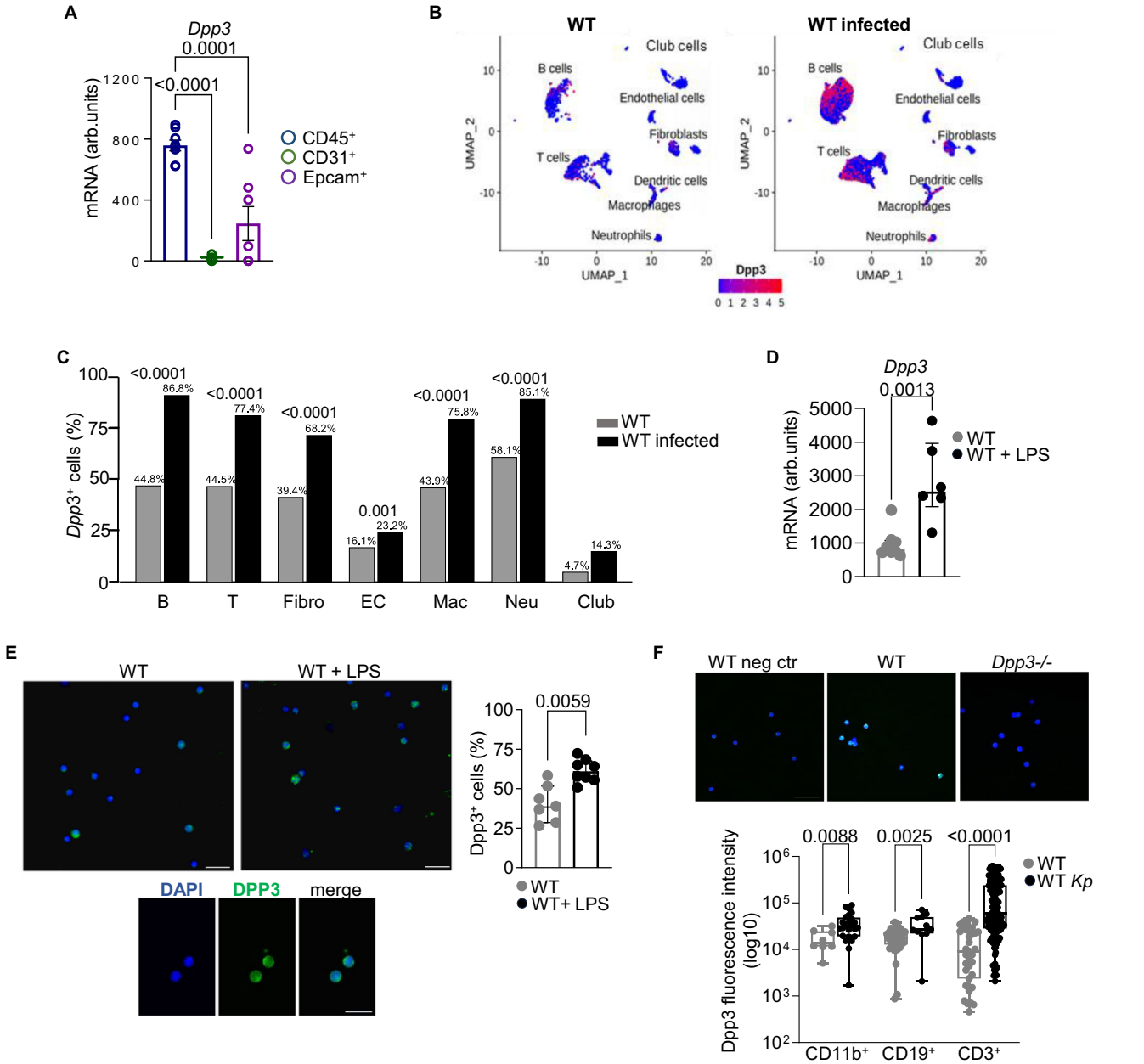


Fig. 4 | Dpp3 is inducible in immune subsets during infection. A *Dpp3* mRNA expression in FACS-sorted lung lymphoid (CD45$^+$), endothelial (CD31$^+$), and epithelial (EpCAM$^+$) cell populations from WT mice ($n = 8$ biological replicates). **B** UMAP plots showing *Dpp3* expression across lung cell types at steady state and following *Kp* infection; expression levels are indicated by the color scale. **C** Quantification of Dpp3$^+$ cells by cell type derived from the UMAP analysis in (**B**). **D** *Dpp3* mRNA expression in total splenocytes from WT mice under steady-state conditions ($n = 8$ biological replicates) or following LPS stimulation ($n = 6$ biological replicates). **E** Representative immunofluorescence staining of Dpp3 in WT splenocytes under basal conditions and 24 h after LPS stimulation. Magnified views show individual channels and merged images (×40, scale bar = 40 µm; ×60, scale bar = 16.7 µm). Bar graph shows the frequency of Dpp3$^+$ splenocytes in untreated ($n = 7$ biological replicates) and LPS-stimulated ($n = 8$ biological replicates) mice. **F** Representative confocal images (×63; scale bar, 36.8 µm) of Dpp3 expression in splenocytes from naive mice. WT negative control (neg ctrl) was obtained by incubation with secondary antibody only. Quantification of Dpp3 protein fluorescence intensity in sorted splenic CD11b$^+$, CD19$^+$, and CD3$^+$ populations from WT mice 48 h after intraperitoneal *Kp* infection and in naive controls ($n = 3$ biological replicates). Data are shown as individual points with mean ± SEM (parametric) or median ± IQR (non-parametric), as indicated. Statistical significance was assessed using one-way ANOVA (**A**), unpaired two-tailed Mann–Whitney *U* test (**D**–**F**), and two-sided Chi-square test (**C**), as appropriate. Nominal *P* values are indicated in the figure. Data represent representative or pooled results from independent experiments. Source data are provided as a Source Data file.

Dpp3 is preferentially expressed in immune-lineage cells and dynamically induced by infection-related signals.

Dpp3 deficiency reshapes baseline lung transcriptome in immune cells

Given the altered pulmonary immune set-point and organized lymphoid architecture observed in *Dpp3*−/− mice under steady-state conditions, we sought to define the molecular basis of this phenotype. RNA-seq analysis of sorted naive CD3$^+$, CD19$^+$, and CD11b$^+$ lung immune subsets revealed extensive transcriptional remodeling across all lineages, with hundreds of genes significantly dysregulated in *Dpp3*-deficient cells (Fig. 5A).

Gene set enrichment analysis (GSEA) demonstrated upregulation of pathways related to oxidative phosphorylation, interferon

https://doi.org/10.1038/s41467-026-74740-3

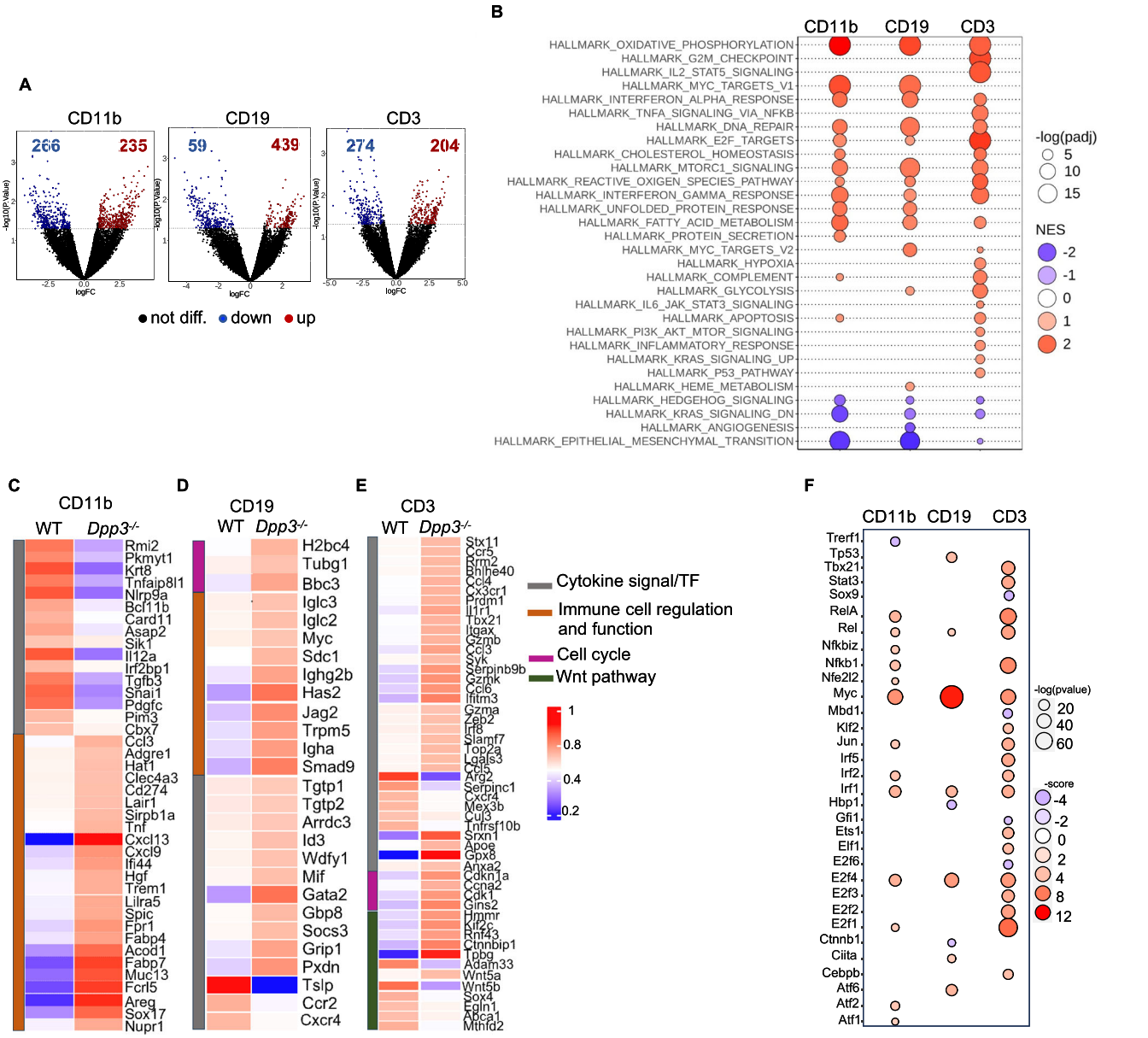


Fig. 5 | Dpp3 deficiency remodels immune transcriptional programs. A Volcano plots showing differentially expressed genes (DEGs) in sorted CD11b$^+$, CD19$^+$, and CD3$^+$ lung immune cell populations from *Dpp3*−/− versus WT mice under steady-state conditions. Differential expression was assessed using limma with an empirical Bayes moderated two-sided *t* test; the *y* axis shows nominal *P* values (no multiple-comparison adjustment). DEGs were defined as $|\log_2 \text{fold change}| > 0.5$ and nominal $P < 0.05$. **B** Gene set enrichment analysis (GSEA) of DEG pathways in the indicated immune populations from *Dpp3*−/− mice relative to WT. Dot size represents statistical significance (Benjamini–Hochberg adjusted *P* value, FDR), and color indicates normalized enrichment score (NES). **C**–**E** Heatmaps of selected DEGs in CD11b$^+$ (**C**), CD19$^+$ (**D**), and CD3$^+$ (**E**) cells, grouped by functional categories related to immune signaling, stress responses, and metabolic regulation. **F** Dot plot depicting transcription factor activity scores inferred using a univariate linear model (ULM) framework. Dot size reflects statistical significance (nominal two-sided *P* value; no multiple-comparison adjustment), and color indicates predicted activity level. RNA-seq analyses were performed on two pooled sample of $n = 3$ mice/group. DEGs were defined as $|\log_2 \text{fold change}| > 0.5$ and $P < 0.05$. Gene set enrichment and transcription factor activity analyses were conducted using the GSEA and decoupleR R packages, respectively.

responses, inflammatory signaling, cell cycle progression and metabolic pathways in *Dpp3*−/− immune cells (Fig. 5B; Supplementary Fig. 9A–C), whereas angiogenesis- and epithelial–mesenchymal transition–associated signatures were relatively reduced (Fig. 5B), consistent with restrained tissue remodeling programs.

Manual inspection of differentially expressed genes highlighted enhanced cytokine signaling and transcription factor activity in CD11b$^+$ cells, including increased expression of *Tnf, Cxcl9*, and *NF-Kb*-related genes, alongside metabolic genes linked to lipid utilization and oxidative stress adaptation (Fig. 5C). Stress-resilience and regenerative factors were also induced[26,27], whereas selected regulators of Th1/Th17 polarization (*Il12a*, *Il17ra*, *Card11*) were relatively reduced, reflecting a reorganization of inflammatory pathway activity (Fig. 5C).

In CD19$^+$ B cells, plasma cell differentiation programs were enriched, consistent with increased expression of *Myc* and *Gata2* and upregulation of Ig transcripts (Fig. 5D). Concomitant reduced expression of *Tslp* (Fig. 5D), a suppressor of germinal center responses, was observed in agreement with derepressed humoral activation.

CD3$^+$ T cells exhibited elevated expression of effector-associated transcription factors such as *Tbx21* and *Prdm1*, together with upregulation of chemokine receptors linked to peripheral tissue homing (Fig. 5E). Modulation of *Wnt/β-catenin* pathway components

implicated in T-cell differentiation and antimicrobial responses[28,29] further supported an activated phenotype (Fig. 5E).

SCENIC-based regulatory network inference[30] identified increased activity of interferon- and NF-κB–associated regulons (*Irf1/2, Rel, Nfkb1, Myc*) across immune subsets (Fig. 5F), supporting coordinated inflammatory priming at baseline[31]. Notably, *Nfe2l2* activity was selectively increased in naive CD11b$^+$ cells (Fig. 5F), linking Dpp3 deficiency to altered redox-sensitive transcriptional regulation[10,32]. In the adaptive compartment, activation-associated regulators such as *Stat3* and *Tbx21* were enriched, whereas suppressive transcriptional programs[33,34] were comparatively reduced (Fig. 5F). B cells displayed increased *Ciita* and *Atf6* activity alongside reduced *Hbp1* (Fig. 5F), consistent with enhanced proliferative and differentiation capacity[35,36].

After confirmation of these transcriptional findings (Supplementary Fig. 10A–C), to validate them at the phenotypic level, lung immune populations were analyzed ex vivo. *Dpp3*−/− mice exhibited increased frequencies of IgA$^+$ plasma cells (Supplementary Fig. 10D), expansion of EM and TE CD4$^+$ and CD8$^+$ T-cell subsets (Supplementary Fig. 10E), and elevated proportions of Tregs (Supplementary Fig. 10F). Consistent with the enriched cell cycle signatures identified by GSEA (Supplementary Fig. 10G), Dpp3-deficient T cells displayed increased Ki67 expression (Supplementary Fig. 10H) and enhanced intracellular IFN-γ production upon stimulation (Supplementary Fig. 10I). Together, these data demonstrate that Dpp3 deficiency establishes a transcriptionally and functionally primed immune landscape in the lung under steady-state conditions.

Dpp3 deficiency alters redox and bioenergetics in immune cells

The transcriptional priming observed in lung-resident immune cells prompted us to determine whether Dpp3 deficiency translates into heightened functional responsiveness upon stimulation. ROS are central regulators of immune activation and antimicrobial responses[37,38]. To assess redox dynamics, we quantified intracellular ROS production in splenocytes following LPS exposure. Both phagocytes and T cells from *Dpp3*−/− mice exhibited significantly elevated ROS levels early after activation compared to WT controls (Fig. 6A). Consistently, extracellular hydrogen peroxide (H_2O_2) release was increased in stimulated Dpp3-deficient cells (Fig. 6B), indicating amplified oxidative responses.

Given the close interplay between redox signaling and inflammatory pathways, we next evaluated NF-κB activation. Dpp3-deficient splenocytes displayed increased NF-κB expression following LPS stimulation (Fig. 6C), accompanied by elevated IFN-γ and IL-6 production and reduced IL-10 levels at 24 h (Fig. 6D). These findings demonstrate that Dpp3 deficiency amplifies inducible inflammatory responses in a cell-intrinsic manner.

To determine whether the amplified redox and inflammatory responses observed in Dpp3-deficient immune cells were supported by metabolic rewiring, we performed untargeted metabolomic profiling of naive splenocytes. Fifty-three metabolites were significantly altered in *Dpp3*−/− cells compared to WT controls (Supplementary Fig. 11A), with the majority exhibiting increased abundance. Pathway enrichment analysis revealed prominent changes in nucleotide metabolism, amino-acid biosynthesis, and glucose-related pathways (Supplementary Fig. 11B).

Accumulation of pentose phosphate pathway intermediates (G6P, S7P, ribulose-5P) together with elevated serine and S-adenosylhomocysteine (SAH) levels indicates increased flux through NADPH-generating and one-carbon metabolic pathways, consistent with heightened redox demand and anabolic support (Supplementary Fig. 11B). Increased intermediates in the hexosamine biosynthetic and purine salvage pathways further suggest enhanced biosynthetic and epigenetic activity (Supplementary Fig. 11B). Elevated glutamine, glutamate, and tricarboxylic acid cycle intermediates were also observed in *Dpp3*−/− cells (Supplementary Fig. 11B). Although reduced expression of selected mitochondrial enzymes (MDH2, OGDH, ACO2) was detected by immunoblotting (Supplementary Fig. 11C), extracellular flux analysis revealed increased basal and maximal mitochondrial respiration in *Dpp3*-deficient splenocytes, accompanied by elevated ATP-linked respiration. Upon LPS stimulation, WT cells exhibited a reduction in oxidative phosphorylation, whereas *Dpp3*−/− cells maintained higher respiratory capacity (Fig. 6E, F).

Together, these findings indicate that Dpp3 deficiency promotes a metabolically primed state characterized by enhanced mitochondrial bioenergetic capacity and redox flux, which in turn boosts inflammatory activation rather than mitochondrial dysfunction.

Dpp3 regulates inducible Nrf2 and signaling networks in infection

To determine whether Dpp3 directly influences redox-sensitive transcriptional control, we first examined its interaction with the Nrf2 inhibitor Keap1. Co-immunoprecipitation experiments demonstrated a physical association between Dpp3 and Keap1 under basal conditions and following LPS stimulation (Supplementary Fig. 12), supporting a stimulus-responsive interaction within the Keap1–Nrf2 regulatory axis. We next examined Nrf2 expression and activation following inflammatory stimulation. *Nrf2* transcript levels did not differ between WT and *Dpp3*−/− splenocytes (Fig. 7A). However, intranuclear Nrf2 protein accumulation was significantly reduced in *Dpp3*-deficient cells within 20–60 min of LPS exposure, as determined by immunofluorescence (Fig. 7B; Supplementary Fig 13). Consistently, Nrf2 transcriptional activity measured by DNA-binding ELISA was significantly impaired in *Dpp3*−/− cells following stimulation, whereas basal activity was only modestly affected (Fig. 7C). These data indicate that Dpp3 regulates inducible Nrf2 stabilization and activation rather than baseline transcription.

To define the broader signaling context of Dpp3 deficiency, we performed label-free quantitative proteomics on WT and *Dpp3*−/− splenocytes under basal and LPS-stimulated conditions. A total of 3333 proteins were identified (Supplementary Data 1) with the majority shared across conditions (Supplementary Fig. 14A). The most pronounced differences were observed between WT and *Dpp3*−/− cells and between WT and WT + LPS samples (Supplementary Fig. 15A; Supplementary Data 2), whereas *Dpp3*−/− proteomic profiles partially overlapped with LPS-stimulated WT cells (Supplementary Fig. 14B–D; Supplementary Fig 15A, B), consistent with a primed inflammatory state.

Pathway enrichment analysis revealed increased abundance of proteins involved in immune signaling, mRNA processing, and membrane trafficking in *Dpp3*−/− cells, while proteins associated with mitochondrial function and apoptosis were comparatively reduced (Supplementary Fig. 15C; Supplementary Data 3). Upregulation of interferon-responsive proteins (e.g., Stat1, Isg15), NF-κB regulators, and redox-associated factors (Gstt2, Park7, Txnl1, Oxsr1) was observed, alongside reduced expression of selected mitochondrial respiratory chain components (Atp5pf, Uqcrc1, Chchd4, Cyc1, Slc25a5) (Fig. 7D, E), consistent with mitochondrial remodeling. Network-based topological analysis of reconstructed protein–protein interaction models identified recurrent hub and bottleneck proteins in Dpp3-deficient conditions, including Myd88 and Mre11, both linked to NF-κB and interferon signaling (Fig. 7F; Supplementary Data 4 and 5**;** Supplementary Fig 16). Shortest-path analysis further identified shared intermediates connecting Dpp3 to Nrf2 and major NF-κB components (Supplementary Figs. 17–19), suggesting that Dpp3 interfaces with proteasome- and ribosome-associated nodes common to both KEAP1–NFE2L2 and NF-κB signaling cascades.

Collectively, these findings indicate that Dpp3 regulates inducible Nrf2 activity while concurrently reshaping inflammatory and proteostasis networks. Rather than functioning as a linear upstream

https://doi.org/10.1038/s41467-026-74740-3

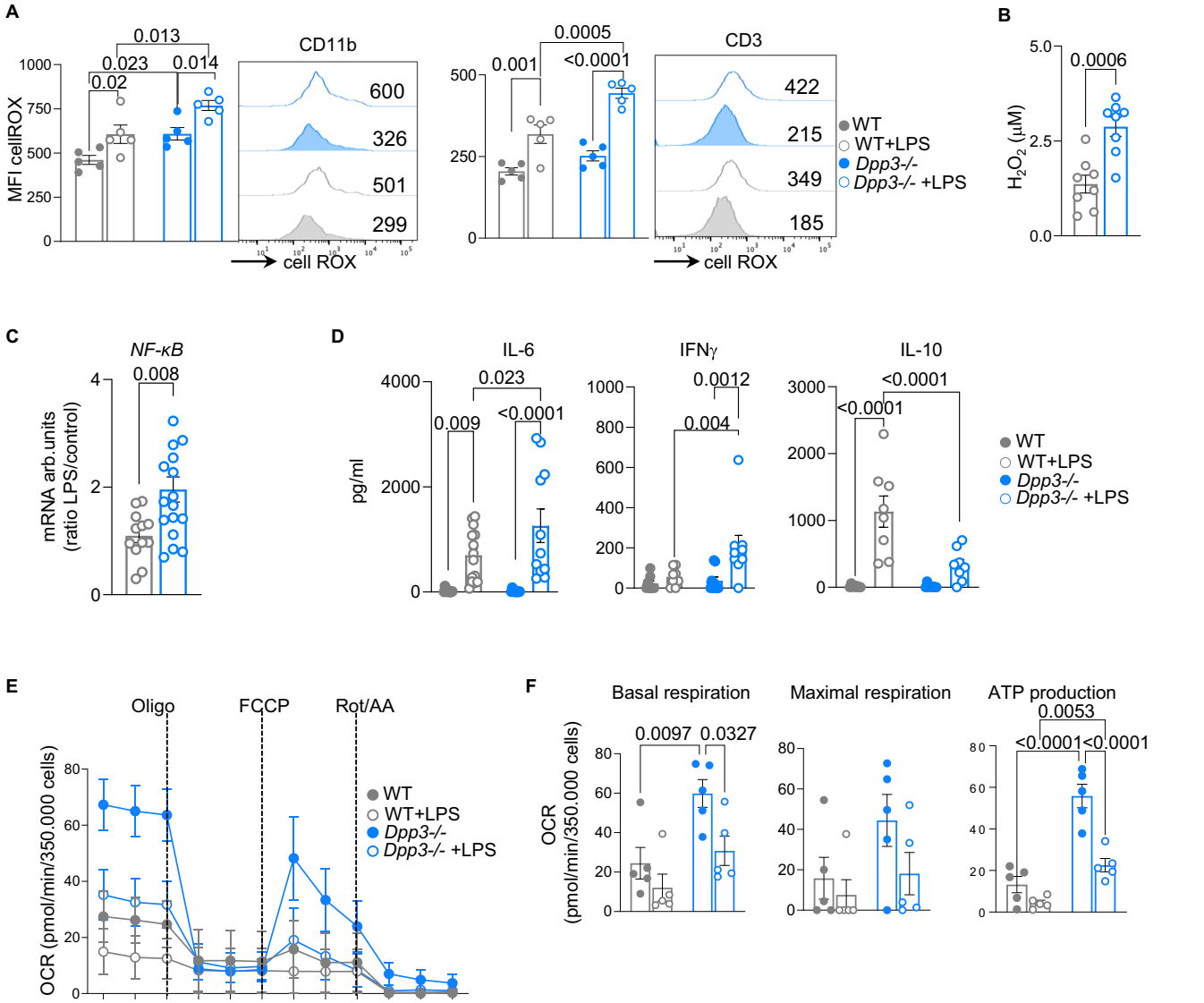


Fig. 6 | Redox and mitochondrial remodeling in Dpp3 deficiency. A Intracellular ROS levels in splenic CD11b$^+$ and CD3$^+$ cells from WT and *Dpp3*−/− mice ($n = 5$) under basal conditions and following LPS stimulation, measured by FACS and expressed as mean fluorescence intensity (MFI). Representative histograms are shown. **B** Extracellular H_2O_2release from WT and *Dpp3*−/− splenocytes following LPS stimulation by ELISA ($n = 8$ biological replicates per group). **C** Relative *NF-Kb* mRNA expression in splenocytes from WT ($n = 10$ biological replicates) and *Dpp3*−/− ($n = 15$ biological replicates) mice following LPS stimulation. **D** Cytokine secretion by splenocytes from WT and *Dpp3*−/− mice under basal conditions and after LPS stimulation (biological replicates: IL-6: WT, $n = 10$; WT LPS, $n = 14$; *Dpp3*−/−, $n = 10$; *Dpp3*−/− LPS, $n = 11$. IFN-γ and IL-10: $n = 8$ for each group). **E** Seahorse extracellular flux analysis of oxygen consumption rate (OCR) in WT and *Dpp3*−/− splenocytes under basal and LPS-stimulated conditions. Seahorse measurements were normalized to cell number per well. Exact *P* values are indicated in the figure. Data derived from analysis of five mice per group. **F** Quantification of basal respiration, maximal respiration and ATP-linked respiration ($n = 5$ biological replicates). Data are presented as individual data points with mean ± SEM. Statistical significance was determined using unpaired two-tailed Student's *t* test (**B**, **C**) or two-way ANOVA (**A**, **D**, **F**), as appropriate. Data represent representative or pooled results from at least two independent experiments. Source data are provided as a Source Data file.

activator, Dpp3 appears to calibrate integrated redox and immune signaling modules that determine the magnitude of inflammatory activation. These integrated data are summarized in the conceptual model presented in Fig. 7G.

Discussion

Our study identifies Dpp3 as a regulator of immune activation thresholds during bacterial infection. Using genetic loss-of-function models, we demonstrate that Dpp3 deficiency enhances bacterial clearance and improves survival in pulmonary and systemic*Kp* infection, while limiting tissue injury and systemic inflammation. These findings extend clinical observations linking elevated circulating Dpp3 with poor outcomes in sepsis[16,17,39] and establish a functional role for Dpp3 in coordinating immune competence and tissue protection in vivo.

Notably, we further demonstrate that Dpp3 expression is broadly induced across innate and adaptive immune subsets during in vivo infection, with particularly robust upregulation in CD3$^+$ T cells. This lineage-specific enhancement aligns with the heightened effector phenotype and IFN-γ production observed in *Dpp3*-deficient T cells, supporting a role for Dpp3 in calibrating adaptive immune activation.

Mechanistically, our data indicate that Dpp3 modulates inducible redox-sensitive signaling rather than constitutively suppressing inflammation, both in ex vivo systems and within the infected pulmonary environment. In immune cells, Dpp3 deficiency impairs stimulus-dependent Nrf2 stabilization and transcriptional activity,

https://doi.org/10.1038/s41467-026-74740-3

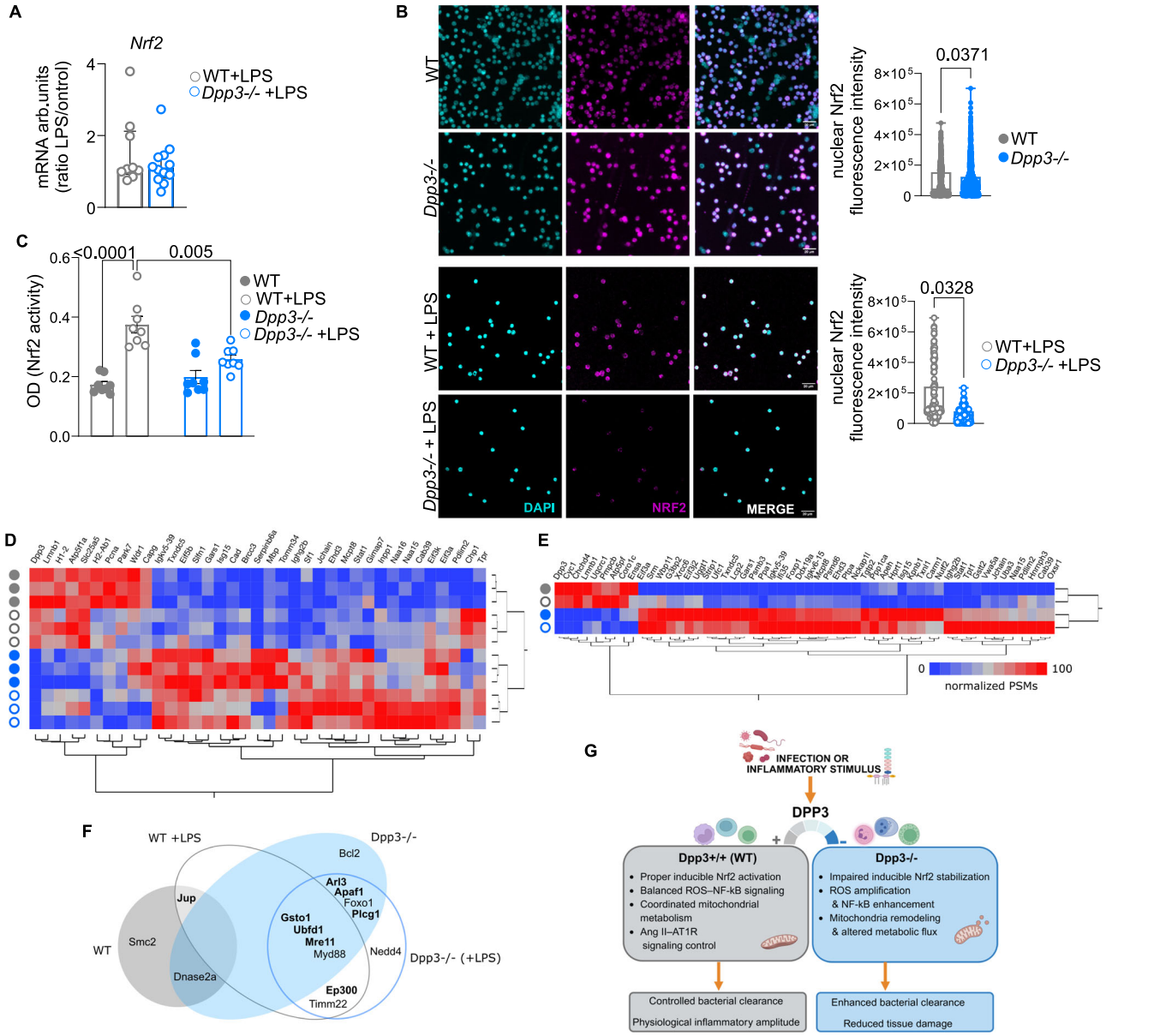


Fig. 7 | Dpp3 calibrates inducible redox and inflammatory signaling. A *Nrf2* mRNA expression in LPS-stimulated splenocytes from WT and *Dpp3−/−* mice (biological replicates: WT, $n = 9$; *Dpp3−/−*, $n = 13$). **B** Representative confocal images (×63, scale bar 20 µm) showing Nrf2 localization (single channels and merged) and quantification of nuclear Nrf2 fluorescence intensity in splenocytes under steady-state conditions and after 20 min LPS stimulation ($n = 3$ biological replicates per group). **C** Nrf2 transcriptional activity measured by ELISA-based ARE-binding assay in WT and *Dpp3−/−* splenocytes under basal and LPS-stimulated conditions ($n = 8$ biological replicates per group). **D** Hierarchical clustering and heatmap of the most significantly differentially expressed proteins (DEPs; $P < 10^{-5}$). **E** Hierarchical clustering and heatmap of DEPs ($P < 0.05$) directly or inversely associated with Dpp3 expression. **F** Venn diagram showing shared and condition-specific hub/bottleneck proteins identified by Betweenness, Bridging, and Centroid centrality analyses; proteins that are also differentially expressed are indicated in bold. **G** Conceptual model of Dpp3-dependent immune activation thresholds. Under physiological conditions, Dpp3 integrates inducible Nrf2 activation, redox balance, mitochondrial metabolism, and Ang II signaling to maintain controlled immune responses. In Dpp3 deficiency, impaired inducible redox regulation and coordinated metabolic remodeling lower immune activation thresholds, enhancing bacterial clearance while limiting tissue damage (Created in BioRender. Ficara F. (2026) https://BioRender.com/c1hrxjn). Data are shown as individual points with mean ± SEM (parametric) or median (non-parametric), as indicated. Statistical analysis: unpaired two-tailed Mann–Whitney *U* test (**A**), two-way ANOVA (**C**), and Wilcoxon test for grouped analyses (**B**), two-sided linear discriminant analysis (**D**, **E**), as appropriate. Exact *P* values are indicated. Proteomic analyses were performed on three biological replicates per condition with technical triplicates. Differentially expressed proteins were defined as $P \leq 0.05$. Network reconstruction and topological analyses were performed using STRING and Cytoscape-based workflows as described in Methods. Source data are provided as a Source Data file.

resulting in amplified ROS accumulation and enhanced NF-κB-associated responses. Importantly, we do not propose Nrf2 as the sole mediator of the phenotype. Instead, proteomic and network analyses reveal coordinated remodeling of interferon signaling, NF-κB regulators, proteostasis components, and mitochondrial proteins, indicating that Dpp3 reshapes a broader inflammatory and proteostasis landscape. Thus, Dpp3 appears to regulate the amplitude of inducible redox and inflammatory programs rather than acting as a linear upstream activator of a single pathway.

This interpretation is supported by our metabolic and bioenergetic analyses. *Dpp3*-deficient immune cells exhibit accumulation of pentose phosphate pathway intermediates and altered one-carbon

metabolism, consistent with increased redox demand and anabolic support. In parallel, reduced expression of selected mitochondrial enzymes together with preserved or enhanced respiratory capacity indicates mitochondrial remodeling rather than bioenergetic failure. Seahorse analyses revealed significant alterations in oxidative phosphorylation parameters, including changes in basal and maximal respiration, supporting mitochondrial remodeling in *Dpp3*-deficient immune cells. In combination with the observed metabolomic shifts, these findings indicate a reprogrammed bioenergetic state rather than uniform metabolic impairment. Collectively, the data suggest that Dpp3 coordinates redox regulation with mitochondrial function and biosynthetic pathways, thereby modulating the amplitude and functional quality of immune activation.

Although Dpp3 deficiency reduces inducible Nrf2 protein levels, the phenotype of *Dpp3*−/− mice differs fundamentally from that of complete Nrf2- or Keap1-deficient models. Whereas global Nrf2 loss is typically associated with impaired host defense and excessive oxidative damage[9,10]. Dpp3 deficiency enhances antimicrobial activity while limiting tissue pathology. This distinction suggests that Dpp3 modulates the dynamics of Nrf2 activation rather than simply suppressing or amplifying the pathway, consistent with a role in calibrating immune responses.

In addition to immune-intrinsic effects, Dpp3 deficiency influences vascular and hormonal responses during infection. Increased Ang II levels and heightened AT1R expression in *Dpp3*−/− mice indicate altered renin–angiotensin system signaling under inflammatory conditions. Pharmacological AT1R blockade abrogated the protective phenotype in Dpp3-deficient mice, supporting the contribution of intact Ang II-AT1R signaling to immune–vascular coordination. Rather than representing an independent mechanism, this axis likely operates within the broader Dpp3-regulated network that integrates inflammatory activation with vascular integrity during sepsis.

Notably, a humanized monoclonal antibody targeting Dpp3 (Procizumab) has been developed and shown to neutralize its enzymatic activity in preclinical and early clinical settings[17]. While previous work has primarily focused on cardiovascular protection, our findings raise the possibility that pharmacologic modulation of Dpp3 may also influence immune activation and metabolic programming during infection. Whether Dpp3 blockade can recapitulate the immunological phenotype observed in Dpp3-deficient mice remains to be determined.

Our findings further support a dual role for Dpp3 in resistance and tolerance. Dpp3 deficiency enhances bacterial clearance while simultaneously reducing inflammatory tissue damage, suggesting improved immune efficiency rather than hyperinflammation. This balance between pathogen elimination and damage control is central to survival during severe infection[40–42]. Whether Dpp3 functions as a molecular node coordinating these complementary defense strategies across tissues warrants further investigation.

Some limitations should be acknowledged. Although adoptive transfer experiments support an immune cell–intrinsic contribution to protection in vivo, the relative quantitative contribution of individual immune subsets remains to be defined using cell-type–specific approaches and does not resolve the relative contribution of tissue-specific immune compartments. In addition, while LPS stimulation provided a controlled and reproducible framework to interrogate Dpp3-dependent immune activation pathways, it does not fully capture the complexity of host–pathogen interactions in the infected lung. Our metabolic and bioenergetic analyses reveal coordinated redox and mitochondrial remodeling, further studies examining temporal dynamics during active infection will clarify how Dpp3-dependent pathways evolve in vivo. Finally, although Ang II–AT1R signaling contributes to the phenotype, the precise balance between immune-intrinsic and vascular mechanisms requires additional dissection.

Our study does not directly address the regulation or functional significance of extracellular Dpp3. Previous reports indicate that Dpp3 may be released during cellular stress[43], but whether circulating Dpp3 exerts active immunomodulatory effects or primarily reflects tissue injury, as previously reported for other DPP family members[33,44–48], remains unclear.

In conclusion, we describe a role for Dpp3 in orchestrating immunometabolic and redox-dependent signaling during infection. By integrating inducible Nrf2 activity, inflammatory network remodeling, mitochondrial function, and hormonal signaling, Dpp3 emerges as a systems-level regulator of immune activation thresholds. These findings highlight Dpp3 as a potential therapeutic target in infectious and inflammatory diseases characterized by dysregulated immune responses.

Methods

Mice

C57BL/6 J wild-type (WT) mice were obtained from Charles River Laboratories (Calco, Italy). *Dpp3*−/− mice were generated as previously described[15] and maintained on a C57BL/6 J background. *Rag1*−/− mice on a C57BL/6 J background were purchased from Charles River Laboratories. Animals were housed under specific pathogen–free conditions at Humanitas Research Hospital (Milan, Italy). Mice were housed under controlled conditions (22 ± 1 °C, 50% humidity, 12 h light/dark cycle) with ad libitum access to food and water. Both male and female mice were used in in vivo experiments. The exact number of animals per sex for each experimental group is provided in the corresponding figure legends. Mice was 8–12 weeks old. Mice were eutanized by CO2 inhalation. All procedures were approved by the Istituto Clinico Humanitas Animal Care and Use Committee (authorization 263/2024-PR) and complied with ARRIVE guidelines.

Infection with bacteria

Klebsiella pneumoniae (*Kp* ATCC 43816) was cultured overnight at 37 °C in Tryptic Soy Broth (BD Biosciences). For pulmonary infection, anesthetized mice received 2×10^2 CFU intranasally in 30 μL PBS. *Pseudomonas aeruginosa* (PAO1) was cultured in LB broth and administered intranasally (1×10^6 CFU in 30 μL PBS). Control mice received PBS alone.

At 48 h post-infection, bacterial burden was quantified in lung homogenates and blood by serial dilution and plating on selective agar, with CFUs determined after overnight incubation at 37 °C. A separate cohort was monitored for 10 days to assess survival.

For systemic infection, 2×10^2 CFU of *Kp* in 100 μL PBS were administered intraperitoneally. At 48 h, livers were harvested, homogenized, serially diluted, and plated for CFU quantification as described above. For pharmacological modulation of AT1R signaling, losartan (PHR1602, Sigma Aldrich) was administered in drinking water (concentration: 600 mg/L) starting 7 days prior to infection and maintained throughout the 48 h post-infection period. Control animals received regular drinking water.

Adoptive transfer transplantation and infection in *Rag1*−/− mice

Total splenocytes (1×10^7) from WT or *Dpp3*−/− females donors were intravenously injected into *Rag1*−/− recipients (CD45 congenic mismatch for tracking). Fifteen hours later, mice were infected intranasally with *Kp*. Forty-eight hours post-infection, bacterial burden and immune reconstitution were assessed.

Tissue processing, flow cytometry, and cell sorting

Spleens and lungs were processed into single-cell suspensions. Lungs were minced and enzymatically digested in HBSS containing Liberase TL (300 μg ml^{-1}; 20 min; 37 °C, Roche cat# 05401020001), filtered through 100 μm strainers in FACS buffer (PBS 1×, 0.5% BSA, 2 mM

EDTA), and centrifuged (290 × *g*, 5 min, RT). Red blood cells were lysed prior to counting. Cells were stained with fluorochrome-conjugated antibodies listed in Supplementary Table 3. Intracellular staining was performed using the Fixation & Permeabilization Buffer Set (ThermoFisher, cat# 88-8824-00). IFN-γ production was assessed after 4 h stimulation with Cell Activation Cocktail plus Brefeldin A (BioLegend, cat# 423303. Ki-67 intranuclear staining was performed ex vivo on unstimulated samples. Viability was assessed with Zombie Aqua Fixable Viability Dye (Biolegend, cat# 423102). Data were acquired on an LSR Fortessa or FACS Symphony A5 (BD) and analyzed in FlowJov.10. Cell sorting was performed using a FACS Aria III (BD). Lung cell populations ($CD45^+$ $EpCam^-$ $CD31^-$; $EpCam^+$ $CD31^-$ $CD45^-$; $CD31^+$ $EpCam^-$ $CD45^-$) and immune subsets ($CD11b^+$, $CD19^+$, $CD3^+$) were purified as indicated.

Functional in vitro assays

To assess cell proliferation, total splenocytes from wild-type (WT) and *Dpp3*−/− mice were resuspended in RPMI 1640 medium supplemented with 10% fetal calf serum (FCS), 2 mM L-glutamine, and 100 IU/ml penicillin/streptomycin. Cells were seeded at 1×10^5 per well in flat-bottom 96-well plates and stimulated with plate-bound anti-mouse CD3 monoclonal antibody (10 µg ml^{-1}, BDPharmingen cat# 553058) and soluble anti-CD28 (2 µg ml^{-1}, BDPharmingen cat# 553295). After 96 h, cultures were pulsed with 0.037 MBq (1 µCi) of [^{3}H]-thymidine (Amersham Pharmacia Biotech) for 14–16 h. Cells were then harvested, and [^{3}H]-thymidine incorporation was measured using a scintillation counter to quantify proliferation. For cytokine measurements, culture supernatants were collected after 48 h from WT and *Dpp3*−/− splenocyte cultures (1.5×10^5 cells/well) stimulated with 10 µg ml^{-1} LPS (Sigma Aldrich, cat# L4005) in round-bottom 96-well plates.

ROS production and phagocytosis assays

Intracellular ROS levels were measured in total splenocytes from WT and *Dpp3*−/− mice using CellROX Deep Red (Thermo Fisher Scientific, cat# C10422; 30 min, 37 °C). ROS production was assessed by flow cytometry in untreated and LPS-stimulated cells (100 µg ml^{-1}, 30 min), as well as in splenocytes isolated from naive and infected mice, and quantified as mean fluorescence intensity (MFI) in gated $CD3^+$ and $CD11b^+$ subsets. Extracellular H_2O_2 release was quantified from culture supernatants of unstimulated or LPS-stimulated splenocytes (10 ng ml^{-1}, 24 h) using a colorimetric ELISA kit (Abcam).

Phagocytic activity was assessed using FITC-conjugated IgG-coated beads (Cayman Chemical, cat# 500290). Splenocytes were incubated with beads (1:200 dilution, 20 min, 37 °C), washed, and fluorescence uptake was quantified by flow cytometry.

ELISA assay

Cytokines (IL-10, IL-6, IL-1β, IL-17, IL-8, MPO, TNF, IFN-γ, CXCL1, CXCL2, CCL3, CCL4, CXCL10, GM-CSF) were measured in undiluted lung homogenates from WT and *Dpp3*−/− mice under basal conditions and 48 h post-infection using mouse DuoSet ELISA kits (R&D Systems; Supplementary Table 4). Selected cytokines (IL-10, IL-6, IL-1β, LTβ4) were also quantified in diluted serum samples.

Plasma DPP3 levels were measured by ELISA (Nordic Biosite, Human cat# OKEH02103; mouse cat# OKEH05715). Serum Ig isotypes (IgG1, IgG2a, IgG2b, IgG3, IgA, IgM) were quantified using a multiplex bead-based assay (Merck Millipore, cat# MGAMMAG-300K) and acquired on a Bio-Plex 200 system (Bio-Rad).

RNA extraction and quantitative real-time PCR

Total RNA was isolated from sorted spleen and lung cells of WT and *Dpp3* −/− mice using QIAzol Lysis Reagent (QIAGEN), according to the manufacturer's protocol. Reverse transcription was performed with the High-Capacity cDNA Reverse Transcription Kit (Applied Biosystems, cat# 4368813). Quantitative real-time PCR was carried out using SYBR Green PCR Master Mix (Bio-Rad, cat# 1725724) in 384-well plates on a ViiA 7 Real-Time PCR System (Applied Biosystems). β-actin was used as the endogenous control for normalization. Primer pairs were selected from the literature when available[15,49], otherwise, they were designed using Primer3web v4.1.0. Primer sequences are listed in Supplementary Table 5.

Bulk RNA sequencing and transcriptomic analysis

RNA libraries from sorted lung cell populations (pooled from three mice per group) were sequenced on an Illumina NextSeq 2000. RNA-seq libraries were prepared using the SMART-Seq v4PLUS Kit User Manual (Takara-Clontech, cat# R400752) according to the manufacturer's instructions. Reads were quality-controlled with FastQC (v0.11.9), aligned to reference genome mm10 using STAR (v2.7.10a)[50]. Read quantification was carried out using the featureCounts function of the Rsubread package (v2.12.3)[51], retaining only uniquely mapping reads. Genes with fewer than 10 counts in at least one sample per cell type and hypervariable genes were filtered out using the DaMiRseq package[52]. Normalization was performed by converting raw counts to logCPM values, followed by variance modeling using the voom function[53]. Batch effects and unwanted variation were corrected with the sva package (v3.46.0)[54]. Differentially expressed genes (DEGs) were identified using the limma package (v3.54.2)[55], applying thresholds of $|\log_2 FC| > 0.5$ and $p < 0.05$. GSEA was conducted using fgsea (v1.24.0) (Korotkevich, "Fast gene set enrichment analysis, bioRxiv, https://doi.org/10.1101/060012, 2021) with the Gene Ontology Biological Process database", excluding pathways with gene set size <10 or $p > 0.05$. Visualizations were generated with ggplot2 (v3.4.4) and ComplexHeatmap (v2.15.3)[56]. Transcription factor activity was inferred using the decoupleR package (v2.6.0)[57] and the CollecTRI network via univariate linear model (ULM).

Single-cell RNA-seq analysis

Publicly available single-cell RNA sequencing data of mouse lung cells were retrieved from the Gene Expression Omnibus (GSE130446 https://www.ncbi.nlm.nih.gov/geo/query/acc.cgi?acc=GSE130446)[25]. Data integration was performed using canonical correlation analysis (CCA) implemented in Seurat v5.0.0[58]. Dimensionality reduction and clustering were conducted using the first 18 principal components, followed by Uniform Manifold Approximation and Projection (UMAP) for visualization.

Cluster annotation was performed by over-representation analysis (ORA) of cluster-specific marker genes identified with the FindAllMarkers function (MAST statistical test)[59], in combination with reference databases including PanglaoDB. Transcription factor activity inference was performed using decoupleR (v2.6.0)[57]. Cells with at least one detected Dpp3 transcript were classified as Dpp3-positive. Cells expressing at least one Dpp3 transcript were classified as Dpp3-positive. For each sample, the proportion of $Dpp3^+$ cells was calculated and normalized to the total number of captured cells to account for variability in sequencing depth and cell loading. Differences in $Dpp3^+$ cell proportions between conditions were evaluated using Fisher's exact test.

Histology and immunohistochemistry

Formalin-fixed, paraffin-embedded (FFPE) mouse tissues were sectioned (1.5 µm) and stained with hematoxylin and eosin (H&E) for histopathological evaluation. For immunohistochemistry, sections were deparaffinized, rehydrated, subjected to antigen retrieval where required, and endogenous peroxidase activity was quenched with 0.3% H_2O_2. Non-specific binding was blocked using Rodent Block (Biocare Medical).

The following primary antibodies were used: anti-CD3 (dilution 1:100; ThermoFisher, cat# MA1-90582), anti-CD45R/B220 (dilution 1:300; ThermoFisher, cat# 14-0452-82), anti-MPO (dilution 1:100;

Abcam, cat# ab9535), anti-Iba1 (dilution 1:300; Fujifilm, cat# 019-19741). Detection was performed using HRP polymer systems (Biocare Medical, cat# MHRP520) with DAB chromogen, followed by hematoxylin counterstaining. Digital images were acquired using an Olympus BX51 microscope equipped with an XC50 camera and processed using CellF Imaging Software.

Histological scoring

Lung tissue damage was evaluated in a double-blind manner by a board-certified histopathologist. For intranasal *Kp* and PAO1 infections, histopathological alterations were scored on a semi-quantitative scale from 0 to 3 (0 = normal; 3 = severe and diffuse cellular infiltration and tissue damage). Individual pathological features were assessed separately, and granulomatous areas were quantified by morphometric analysis (Image Pro Premier) on digital slides acquired using an Olympus VS120-L100 scanner. The following scoring system was applied: 0 = normal condition; ≥0.5 to < 1 = mild tissue damage with diffuse cellularity (no clustering); ≥1 to < 2 = low and focal cellular infiltration/tissue damage; ≥2 to < 3 = moderate cellular infiltration/tissue damage; ≥ 3 = severe and diffuse cellular infiltration/tissue damage.

For i.p. *Kp* infection, a separate scoring system was applied to quantify hemorrhagic injury. The severity of alveolar, bronchial, and vascular hemorrhages was individually evaluated and summed to obtain a cumulative hemorrhage score (range 0–3), defined as: 0 = normal condition; ≥0.5 to < 1 = very mild hemorrhage and tissue injury; ≥1 to < 2 = low and focal hemorrhage and tissue injury; ≥2–< 3 = moderate and partial hemorrhage and tissue injury; ≥3 = severe and diffuse hemorrhage and tissue injury.

Extracellular flux analysis

Mitochondrial respiration and glycolytic function were assessed using a Seahorse XFe96 analyzer (Agilent). Splenocytes were plated at 4×10^5 cells/well on Cell-Tak–coated XF96 plates (Agilent, cat# 103798-100) and equilibrated for 1 h at 37 °C in a non-CO_2 incubator in complete XF Base Medium (pH 7.4)(Agilent, cat# 103335). Where indicated, cells were stimulated with LPS (100 μg ml^{-1}, 1 h) prior to the assay. Oxygen consumption rate (OCR) was measured using the XF Cell Mito Stress Test (Agilent, cat# 103015-100) with sequential injection of oligomycin (1.5 μM), FCCP (2 μM), and rotenone/antimycin A (0.5 μM). Basal respiration, maximal respiration, spare respiratory capacity, and ATP-linked respiration were calculated using Wave software version 2.6.4.24 (Agilent Technologies), according to the manufacturer's instructions. Data were normalized to cell number. Experiments included five biological replicates per condition and three technical replicates per sample.

Immunofluorescence

For immunofluorescence staining, 2×10^5 total splenocytes were stimulated with LPS as follows: 10 μg ml^{-1}, 24 h for Dpp3 detection, and 100 μg ml^{-1}, 1 h for Nrf2 analysis. Unstimulated cells cultured in medium alone served as controls. Following stimulation, cells were harvested, cytospun onto glass slides, and fixed in 4% paraformaldehyde. Permeabilization and blocking were performed using 0.3% Triton X-100 and 1% BSA in PBS. Slides were then incubated with the following Abcam primary antibodies: anti-Dpp3 (dilution 1:100, Abcam cat# ab97437) and anti-Nrf2 (dilution 1:1000, Proteintech cat# 16396-I-AP). After washing, cells were incubated with Alexa Fluor 488-conjugated secondary antibodies (dilution 1:1000, Life Technologies) and counterstained with DAPI (200 μg ml^{-1}). Images were acquired using a cooled CCD camera mounted on an Olympus BX61 fluorescence microscope and analyzed with CytoVision software (Applied Imaging).

Confocal analysis

Images were acquired using a Leica SP8i confocal laser scanning microscope equipped with a ×63/1.4 NA oil immersion objective. DAPI and FITC were excited at 405 nm and 488 nm, respectively. Z-stacks were collected at 0.4 μm intervals to encompass the full cellular volume. For each sample (n = 3–5 mice per genotype and condition), at least five fields of view were acquired, corresponding to ~35–70 cells per condition.

Acquisition parameters, including laser power and detector gain, were optimized and kept constant across all samples within each experiment. Image analysis was performed using Imaris (Bitplane) for 3D reconstruction and quantitative measurements, and Fiji (ImageJ 2.16.0) for additional processing.

Fluorescence quantification was based on integrated (sum) intensity measurements. For Nrf2 nuclear localization, z-stack images were acquired under identical settings across conditions. 3D reconstructions were generated, and nuclear regions of interest (ROIs) were defined by segmentation of the DAPI channel. Binary masks derived from DAPI staining were applied to restrict analysis to nuclear compartments. The integrated Nrf2 fluorescence intensity within DAPI-positive regions was quantified on a per-cell basis.

For Dpp3 analysis, fluorescence intensity was quantified without nuclear segmentation. Images were acquired under identical settings across all samples, and regions of interest corresponding to individual cells were defined. The integrated Dpp3 fluorescence intensity was measured for each ROI and used for comparative analysis across conditions. Imaging parameters were set to minimize background and maintained constant across genotypes; *Dpp3*−/− samples were used to assess background signal levels.

Nrf2 transcriptional activity assay (DNA-binding ELISA)

Nrf2 transcriptional activity was assessed using a colorimetric-based DNA-binding assay (ARE-binding; Abcam, cat# ab207223). WT and *Dpp3*−/− splenocytes (10×10^6 cells) were left unstimulated or stimulated with LPS (100 μg ml^{-1}, 1 h), and nuclear extracts were prepared (Abcam, cat# ab113474). Equal amounts of nuclear protein (5 μg/well) were incubated on ARE-coated plates, and bound Nrf2 was detected with kit-provided antibodies and HRP/TMB development. Absorbance was read at 450 nm and expressed after blank subtraction. Experiments were performed with at least 3 biological replicates and technical duplicates.

Protein extraction and nanoLC–HRMS/MS analysis

Total splenocytes (15×10^6 cells) were stimulated with LPS (100 μg ml^{-1}, 1 h) or left untreated. Cells were washed, pelleted, and stored at −80 °C. Pellets were lysed using Universal Nuclease and Lysis Solution (Thermo Fisher Scientific cat# 88702), and protein concentration was determined by Qubit Protein Assay (Thermo Fisher Scientific, cat# Q33211). For each sample, 50 μg of protein were reduced, alkylated, and digested with Trypsin/Lys-C, followed by clean-up using the EasyPep Mini MS Sample Preparation Kit (Thermo Fisher Scientific, cat# 15947032). Peptides were reconstituted in 0.1% formic acid and diluted to 0.1 μg μl^{-1} before analysis.

Peptide separation was performed on a Vanquish Neo UHPLC system (Thermo Fisher Scientific) equipped with PepMap Neo trap and analytical columns (75 μm I.D., 15 cm), using a 60-min gradient from 4% to 70% acetonitrile in 0.1% formic acid at 300 nL/min. Peptides were separated using a 60-minute gradient: 4–5% B (1 min), 5–29% B (37 min), 29–50% B (20 min), and 50–70% B (1 min), followed by column washing at 99% B for 5 min. The flow rate during gradient elution was maintained at 300 nL/min. Mass spectrometry was carried out on an Orbitrap Exploris 240 (Thermo Fisher Scientific) operating in data-dependent acquisition (Top20) mode. Three biological replicates per condition (WT, *Dpp3*−/−, WT + LPS, *Dpp3*−/− + LPS) were analyzed in triplicate technical runs (36 total LC–MS/MS runs).

Raw mass spectra data processing

Raw mass spectra were processed using Proteome Discoverer v2.5 (Thermo Fisher Scientific, San Jose, CA, USA). Processing and Consensus Workflows were configured for protein identification and functional annotation (see Supplementary Methods). The *Mus musculus* protein database was retrieved from UniProt (January 2026 release). Trypsin was specified as the digestion enzyme. Carbamidomethylation of cysteine residues was set as a fixed modification, and methionine oxidation as a variable modification. Peptide charge states from 2 to 6 were considered. Precursor mass tolerance was set to 10 ppm and fragment mass tolerance to 0.02 Da. The false discovery rate (FDR) threshold was set at 1% (strict).

Label-free quantitative analysis

Label-free semi-quantitative analysis was performed as previously described[60]. Peptide Spectrum Matches (PSMs) were normalized using total signal normalization. The resulting data matrix (36 samples, 3333 proteins) was subjected to two-sided Linear Discriminant Analysis (LDA), and proteins with $P \leq 0.05$ were selected as differentially expressed proteins (DEPs) in pairwise comparisons (WT vs *Dpp3−/−*; WT + LPS vs *Dpp3−/−* + LPS; WT vs WT + LPS; *Dpp3−/−* vs *Dpp3−/−* + LPS). Selected DEPs were further evaluated using the DAve index. Hierarchical clustering, principal component analysis (PCA), and Spearman's correlation analysis were subsequently performed. Data processing was carried out using JMP 17 statistical software and in-house R scripts.

Enrichment analysis

DEPs were functionally analyzed as previously reported[61]. For each pairwise comparison, up- and down-regulated proteins were analyzed separately. Enrichment of GO Biological Process (BP), GO Molecular Function (MF), GO Cellular Component (CC), KEGG, Reactome, and WikiPathways terms (FDR ≤ 0.01) was performed using the STRING functional annotation tool[62]. Terms enriched in both up- and down-regulated sets were excluded to retain direction-specific enrichment signatures.

Reconstruction of PPI network models: topological analysis and hub/bottleneck selection

Condition-specific *Mus musculus* protein–protein interaction (PPI) networks were reconstructed using the STRING Cytoscape app[62], based on proteins identified by nanoLC–HRMS/MS analysis (WT: 2838; *Dpp3−/−*: 3199; WT + LPS: 3111; *Dpp3−/−*+LPS: 3189). Only interactions annotated as "databases" and/or "experiments" with a confidence score ≥0.3 were retained. Topological analysis was performed using the CentiScaPe Cytoscape app[63]. Betweenness, Centroid, and Bridging centralities were calculated to identify hub and bottleneck nodes[64]. Statistical significance was assessed using randomized network models[65]. For each condition, 100 random networks were generated and analyzed using in-house R scripts based on the VertexSort, igraph, and ggplot2 libraries. Shortest paths between selected node pairs were extracted using the Pesca Cytoscape app[66].

Statistical analysis

Statistical analyses were performed using GraphPad Prism v10 (GraphPad Software). Normality was assessed using the Shapiro–Wilk test. Parametric data were analyzed using unpaired two-tailed Student's *t* test, and non-parametric data using the Mann–Whitney U test. Categorical variables were compared using the Chi-square test on contingency tables. Survival curves were analyzed by Kaplan–Meier method and compared using the log-rank (Mantel–Cox) test. Data are presented as mean ± SEM (parametric) or median ± IQR (non-parametric), with individual data points shown. Sample sizes (*n*), statistical tests, and significance thresholds are specified in the figure legends. A two-tailed *P* value ≤ 0.05 was considered statistically significant.

Reporting summary

Further information on research design is available in the Nature Portfolio Reporting Summary linked to this article.

Data availability

The raw total RNA sequencing data generated in this study have been deposited in the GEO under accession code GSE320460. Raw MS proteomics data are available at ProteomeXchange Consortium via the PRIDE partner repository with the dataset identified PXD074007. The source data underlying the main figures and relevant Supplementary Figs. are provided as a Source Data file. All other data supporting the findings of this study are available within the Article, Supplementary Information, and Supplementary Data or from the authors upon reasonable request. Source data are provided with this paper.

References

1. Singer, M. et al. The third international consensus definitions for sepsis and septic shock (sepsis-3). *JAMA* **315**, 801–810 (2016).
2. Hotchkiss, R. S. & Moldawer, L. L. Parallels between cancer and infectious disease. *N. Engl. J. Med.* **371**, 380–383 (2014).
3. Garduno A., Martín-Loeches I. Targeting sepsis: disease tolerance, immune resilience, and compartmentalized immunity. *Biomedicines* **12**, 2420 (2024).
4. Pearce, E. L. & Pearce, E. J. Metabolic pathways in immune cell activation and quiescence. *Immunity* **38**, 633–643 (2013).
5. Nathan, C. & Cunningham-Bussel, A. Beyond oxidative stress: an immunologist's guide to reactive oxygen species. *Nat. Rev. Immunol.* **13**, 349–361 (2013).
6. Yamamoto, M., Kensler, T. W. & Motohashi, H. The KEAP1-NRF2 system: a thiol-based sensor-effector apparatus for maintaining redox homeostasis. *Physiol. Rev.* **98**, 1169–1203 (2018).
7. Ryan, D. G. et al. Nrf2 activation reprograms macrophage intermediary metabolism and suppresses the type I interferon response. *iScience* **25**, 103827 (2022).
8. Mitsuishi, Y. et al. Nrf2 redirects glucose and glutamine into anabolic pathways in metabolic reprogramming. *Cancer Cell* **22**, 66–79 (2012).
9. Kobayashi, E. H. et al. Nrf2 suppresses macrophage inflammatory response by blocking proinflammatory cytokine transcription. *Nat. Commun.* **7**, 11624 (2016).
10. Thimmulappa, R. K. et al. Nrf2 is a critical regulator of the innate immune response and survival during experimental sepsis. *J. Clin. Invest.* **116**, 984–995 (2006).
11. Baral, P. K. et al. The first structure of dipeptidyl-peptidase III provides insight into the catalytic mechanism and mode of substrate binding. *J. Biol. Chem.* **283**, 22316–22324 (2008).
12. Picod, A. et al. Circulating dipeptidyl peptidase 3 modulates systemic and renal hemodynamics through cleavage of angiotensin peptides. *Hypertension* **81**, 927–935 (2024).
13. Malovan, G. et al. The emerging role of dipeptidyl peptidase 3 in pathophysiology. *FEBS J.* **290**, 2246–2262 (2023).
14. Lu, K. et al. NRF2 induction supporting breast cancer cell survival is enabled by oxidative stress-induced DPP3-KEAP1 interaction. *Cancer Res.* **77**, 2881–2892 (2017).
15. Menale, C. et al. Absence of dipeptidyl peptidase 3 increases oxidative stress and causes bone loss. *J. Bone Min. Res.* **34**, 2133–2148 (2019).
16. Dépret, F. et al. Circulating dipeptidyl peptidase-3 at admission is associated with circulatory failure, acute kidney injury and death in severely ill burn patients. *Crit. Care* **24**, 168 (2020).
17. Garcia, B. et al. Inhibition of circulating dipeptidyl-peptidase 3 by procizumab in experimental septic shock reduces catecholamine exposure and myocardial injury. *Intensive Care Med. Exp.* **12**, 53 (2024).

18. Ye, P. et al. DPP3: from biomarker to therapeutic target of cardiovascular diseases. *Front. Cardiovasc. Med.* **9**, 974035 (2022).
19. Frigyesi, A. et al. Circulating dipeptidyl peptidase 3 on intensive care unit admission is a predictor of organ dysfunction and mortality. *J. Intensive Care* **9**, 52 (2021).
20. Picod, A. et al. High circulating dipeptidyl peptidase 3 predicts mortality and need for organ support in cardiogenic shock: an ancillary analysis of the ACCOST-HH trial. *J. Card. Fail.* **31**, 29–36 (2025).
21. Perlee, D. et al. Human adipose-derived mesenchymal stem cells modify lung immunity and improve antibacterial defense in pneumosepsis caused by Klebsiella pneumoniae. *Stem Cells Transl. Med.* **8**, 785–796 (2019).
22. Osherov, N. & Ben-Ami, R. Modulation of host angiogenesis as a microbial survival strategy and therapeutic target. *PLoS Pathog.* **12**, e1005479 (2016).
23. Brandt, S. L. & Serezani, C. H. Too much of a good thing: how modulating LTB_4 actions restore host defense in homeostasis or disease. *Semin. Immunol.* **33**, 37–43 (2017).
24. van Lier, D., Kox, M. & Pickkers, P. Promotion of vascular integrity in sepsis through modulation of bioactive adrenomedullin and dipeptidyl peptidase 3. *J. Intern. Med.* **289**, 792–806 (2021).
25. Amezcua Vesely, M. C. et al. Effector TH17 cells give rise to long-lived TRM cells that are essential for an immediate response against bacterial infection. *Cell* **178**, 1176–88.e15 (2019).
26. Liu, J. et al. NUPR1 is a critical repressor of ferroptosis. *Nat. Commun.* **12**, 647 (2021).
27. Liu, M. et al. Sox17 is required for endothelial regeneration following inflammation-induced vascular injury. *Nat. Commun.* **10**, 2126 (2019).
28. Blumenthal, A. et al. The Wingless homolog WNT5A and its receptor Frizzled-5 regulate inflammatory responses of human mononuclear cells induced by microbial stimulation. *Blood* **108**, 965–973 (2006).
29. Jeannet, G. et al. Essential role of the Wnt pathway effector Tcf-1 for the establishment of functional CD8 T cell memory. *Proc. Natl. Acad. Sci. USA* **107**, 9777–9782 (2010).
30. Aibar, S. et al. SCENIC: single-cell regulatory network inference and clustering. *Nat. Methods* **14**, 1083–1086 (2017).
31. Huber, J. P. & Farrar, J. D. Regulation of effector and memory T-cell functions by type I interferon. *Immunology* **132**, 466–474 (2011).
32. Daskou, M. et al. The role of the NRF2 pathway in the pathogenesis of viral respiratory infections. *Pathogens* **13**, 39 (2023).
33. Zhong, H. et al. SOX9 drives KRAS-induced lung adenocarcinoma progression and suppresses anti-tumor immunity. *Oncogene* **42**, 2183–2194 (2023).
34. Waterfield, M. et al. The transcriptional regulator Aire coopts the repressive ATF7ip-MBD1 complex for the induction of immunotolerance. *Nat. Immunol.* **15**, 258–265 (2014).
35. Bollaert, E., de Rocca Serra, A. & Demoulin, J. B. The HMG box transcription factor HBP1: a cell cycle inhibitor at the crossroads of cancer signaling pathways. *Cell Mol. Life Sci.* **76**, 1529–1539 (2019).
36. Gass, J. N., Gifford, N. M. & Brewer, J. W. Activation of an unfolded protein response during differentiation of antibody-secreting B cells. *J. Biol. Chem.* **277**, 49047–49054 (2002).
37. Shekhova, E. Mitochondrial reactive oxygen species as major effectors of antimicrobial immunity. *PLoS Pathog.* **16**, e1008470 (2020).
38. Sena, L. A. et al. Mitochondria are required for antigen-specific T cell activation through reactive oxygen species signaling. *Immunity* **38**, 225–236 (2013).
39. Ventoulis, I. et al. Bio-adrenomedullin and dipeptidyl peptidase 3 as novel sepsis biomarkers in the emergency department and the intensive care unit: a narrative review. *Medicina* **61**, 1059 (2013).
40. Martins, R. et al. Disease tolerance as an inherent component of immunity. *Annu. Rev. Immunol.* **37**, 405–437 (2019).
41. Soares, M. P., Teixeira, L. & Moita, L. F. Disease tolerance and immunity in host protection against infection. *Nat. Rev. Immunol.* **17**, 83–96 (2017).
42. Chovatiya, R. & Medzhitov, R. Stress, inflammation, and defense of homeostasis. *Mol. Cell* **54**, 281–288 (2014).
43. Wattiaux, R., Wattiaux-de Coninck, S., Thirion, J., Gasingirwa, M. C. & Jadot, M. Lysosomes and Fas-mediated liver cell death. *Biochem J.* **403**, 89–95 (2007).
44. Palmér, R. et al. Dipeptidyl peptidase 1 inhibitor AZD7986 induces a sustained, exposure-dependent reduction in neutrophil elastase activity in healthy subjects. *Clin. Pharm. Ther.* **104**, 1155–1164 (2018).
45. Zhong, F. L. et al. Human DPP9 represses NLRP1 inflammasome and protects against autoinflammatory diseases via both peptidase activity and FIIND domain binding. *J. Biol. Chem.* **293**, 18864–18878 (2018).
46. Zhang, H., Chen, Y., Keane, F. M. & Gorrell, M. D. Advances in understanding the expression and function of dipeptidyl peptidase 8 and 9. *Mol. Cancer Res.* **11**, 1487–1496 (2013).
47. Huang, J. et al. Emerging role of dipeptidyl peptidase-4 in autoimmune disease. *Front. Immunol.* **13**, 830863 (2022).
48. Waumans, Y., Baerts, L., Kehoe, K., Lambeir, A. M. & De Meester, I. The dipeptidyl peptidase family, prolyl oligopeptidase, and prolyl carboxypeptidase in the immune system and inflammatory disease, including atherosclerosis. *Front. Immunol.* **6**, 387 (2015).
49. Rigoni, R. et al. Cutaneous barrier leakage and gut inflammation drive skin disease in Omenn syndrome. *J. Allergy Clin. Immunol.* **146**, 1165–1179.e11 (2020).
50. Dobin, A. et al. STAR: ultrafast universal RNA-seq aligner. *Bioinformatics* **29**, 15–21 (2013).
51. Liao, Y., Smyth, G. K. & Shi, W. The R package Rsubread is easier, faster, cheaper and better for alignment and quantification of RNA sequencing reads. *Nucleic Acids Res.* **47**, e47 (2019).
52. Chiesa, M., Colombo, G. I. & Piacentini, L. DaMiRseq-an R/Bioconductor package for data mining of RNA-Seq data: normalization, feature selection and classification. *Bioinformatics* **34**, 1416–1418 (2018).
53. Law, C. W., Chen, Y., Shi, W. & Smyth, G. K. voom: precision weights unlock linear model analysis tools for RNA-seq read counts. *Genome Biol.* **15**, R29 (2014).
54. Leek, J. T., Johnson, W. E., Parker, H. S., Jaffe, A. E. & Storey, J. D. The sva package for removing batch effects and other unwanted variation in high-throughput experiments. *Bioinformatics* **28**, 882–883 (2012).
55. Ritchie, M. E. et al. limma powers differential expression analyses for RNA-sequencing and microarray studies. *Nucleic Acids Res.* **43**, e47 (2015).
56. Gu, Z., Eils, R. & Schlesner, M. Complex heatmaps reveal patterns and correlations in multidimensional genomic data. *Bioinformatics* **32**, 2847–2849 (2016).
57. Badia-I-Mompel, P. et al. decoupleR: ensemble of computational methods to infer biological activities from omics data. *Bioinform. Adv.* **2**, vbac016 (2022).
58. Hao, Y. et al. Dictionary learning for integrative, multimodal and scalable single-cell analysis. *Nat. Biotechnol.* **42**, 293–304 (2024).
59. Finak, G. et al. MAST: a flexible statistical framework for assessing transcriptional changes and characterizing heterogeneity in single-cell RNA sequencing data. *Genome Biol.* **16**, 278 (2015).
60. Di Silvestre, D., Brambilla, F., Merlini, G. & Mauri, P. Computational tools and methods for the study of systemic amyloidosis at the clinical and molecular level. *Methods Mol. Biol.* **2884**, 369–387 (2025).
61. Lomagno A. et al. CoPPIs algorithm: a tool to unravel protein cooperative strategies in pathophysiological conditions. *Brief. Bioinform.* **26**, bbaf146 (2025).

62. Szklarczyk, D. et al. The STRING database in 2021: customizable protein-protein networks, and functional characterization of user-uploaded gene/measurement sets. *Nucleic Acids Res.* **49**, D605–D612 (2021).
63. Scardoni, G. et al. Biological network analysis with CentiScaPe: centralities and experimental dataset integration. *F1000Res* **3**, 139 (2014).
64. Sereni, L. et al. Lentiviral gene therapy corrects platelet phenotype and function in patients with Wiskott-Aldrich syndrome. *J. Allergy Clin. Immunol.* **144**, 825–838 (2019).
65. Tosadori, G., Bestvina, I., Spoto, F., Laudanna, C. & Scardoni, G. Creating, generating and comparing random network models with NetworkRandomizer. *F1000Res* **5**, 2524 (2016).
66. Scardoni, G., Tosadori, G., Pratap, S., Spoto, F. & Laudanna, C. Finding the shortest path with PesCa: a tool for network reconstruction. *F1000Res* **4**, 484 (2015).

Acknowledgements

We thank Maria Fumagalli from the Imaging Facility and the Flow Cytometry Core of Humanitas Research Hospital for experimental support.

Author contributions

Conceptualization: Am.F., L.L., F.G., V.M., and B.C. Investigation: Am.F., L.L., E.F., F.N., M.L.S., D.S., R.V., F.B., An.F., M.M., D.Mo., S.M., M.B., G.R., C.M., V.M. Resources: D.Ma., C.G., Y.T., A.M., A.B., D.G., C.S., S.S., C.P., P.M., D.D.S. Writing: Am.F., L.L., D.D.S., F.G., V.M., and B.C. Funding acquisition, F.G. and B.C.; supervision, F.G., V.M., and B.C.

Funding

This work was supported by a grant from the European Union Next Generation EU, Mission 4 Component 1 CUP H53D23000630006 to F.G. and B.C; by the "Fondo di Sostegno alla Ricerca" (Departmental Research Fund) of the Department. BIOMETRA, University of Milan, to B.C. This work was also partially supported by grants from the Italian Ministry of Health (GR-2016-02362572 to B.C and A.M.; PNRR-MAD-2022-12376828 to Y.T.). A.F. is the recipient of AFM-Telethon–Plateforme Maladies Rares (Application number 24382). The authors acknowledge the support of the APC central fund of the University of Milan.

Competing interests

The authors declare no competing interests.

Additional information

Supplementary information The online version contains supplementary material available at https://doi.org/10.1038/s41467-026-74740-3.

Correspondence and requests for materials should be addressed to Barbara Cassani.

Peer review information *Nature Communications* thanks the anonymous reviewer(s) for their contribution to the peer review of this work. A peer review file is available.

Reprints and permissions information is available at http://www.nature.com/reprints

Publisher's note Springer Nature remains neutral with regard to jurisdictional claims in published maps and institutional affiliations.

Open Access This article is licensed under a Creative Commons Attribution-NonCommercial-NoDerivatives 4.0 International License, which permits any non-commercial use, sharing, distribution and reproduction in any medium or format, as long as you give appropriate credit to the original author(s) and the source, provide a link to the Creative Commons licence, and indicate if you modified the licensed material. You do not have permission under this licence to share adapted material derived from this article or parts of it. The images or other third party material in this article are included in the article's Creative Commons licence, unless indicated otherwise in a credit line to the material. If material is not included in the article's Creative Commons licence and your intended use is not permitted by statutory regulation or exceeds the permitted use, you will need to obtain permission directly from the copyright holder. To view a copy of this licence, visit http://creativecommons.org/licenses/by-nc-nd/4.0/.

© The Author(s) 2026

[1]Humanitas University, Milan, Italy. [2]IRCCS Humanitas Research Hospital, Milan, Italy. [3]Bioinformatics Unit, IRCCS Humanitas Research Hospital, Milan, Italy. [4]Dep. Medical Biotechnology and Translational Medicine (BIOMETRA), University of Milan, Milan, Italy. [5]Institute for Genetic and Biomedical Research, Milan, Italy. [6]Institute for Biomedical Technologies (ITB), National Research Council (CNR), Milan, Italy. [7]Infectious Diseases Unit, Foundation IRCCS Ca' Granda Ospedale Maggiore Policlinico, Milan, Italy. [8]San Raffaele-Telethon Institute for Gene Therapy (SR-TIGET), IRCCS San Raffaele Scientific Institute, Milan, Italy. [9]Institute of Bioimaging and Biological Complex Systems (IBSBC), National Research Council (CNR), Milan, Italy. [10]Neurology Unit, Fondazione IRCCS Ca' Granda Ospedale Maggiore Policlinico, Milan, Italy. [11]Stem Cell Laboratory, Dino Ferrari Center, Department of Pathophysiology and Transplantation, Università degli Studi di Milano, Milan, Italy. [12]Dep. of Biotechnology and Biosciences, University of Milano Bicocca, Milan, Italy. [13]Dep. of Clinical Medicine and Surgery, University of Naples "Federico II", Naples, Italy. [14]Dep. of Pathophysiology and Transplantation, University of Milan, Milan, Italy. [15]Human Technopole, Via Rita levi Montalcini 1, Milan, Italy. [16]These authors contributed equally: Amanda Facoetti, Luca Lambroia. [17]These authors jointly supervised this work: Veronica Marrella, Barbara Cassani. ✉e-mail: barbara.cassani@unimi.it